

The MASSIVE Survey - VII. The Relationship of Angular Momentum, Stellar Mass and Environment of Early-Type Galaxies

Melanie Veale,^{1,2★} Chung-Pei Ma,^{1,2★} Jenny E. Greene,³ Jens Thomas,⁴
John P. Blakeslee,⁵ Nicholas McConnell,⁵ Jonelle L. Walsh,⁶ Jennifer Ito¹

¹*Department of Astronomy, University of California, Berkeley, CA 94720, USA*

²*Department of Physics, University of California, Berkeley, CA 94720, USA*

³*Department of Astrophysical Sciences, Princeton University, Princeton, NJ 08544, USA*

⁴*Max Planck-Institute for Extraterrestrial Physics, Giessenbachstr. 1, D-85741 Garching, Germany*

⁵*Dominion Astrophysical Observatory, NRC Herzberg Astronomy and Astrophysics, Victoria BC V9E2E7, Canada*

⁶*George P. and Cynthia Woods Mitchell Institute for Fundamental Physics and Astronomy, and Department of Physics and Astronomy, Texas A&M University, College Station, TX 77843, USA*

Accepted XXX. Received YYY; in original form ZZZ

ABSTRACT

We analyse the environmental properties of 370 local early-type galaxies (ETGs) in the MASSIVE and ATLAS^{3D} surveys, two complementary volume-limited integral-field spectroscopic (IFS) galaxy surveys spanning absolute K -band magnitude $-21.5 \gtrsim M_K \gtrsim -26.6$, or stellar mass $8 \times 10^9 \lesssim M_* \lesssim 2 \times 10^{12} M_\odot$. We find these galaxies to reside in a diverse range of environments measured by four methods: group membership (whether a galaxy is a brightest group/cluster galaxy, satellite, or isolated), halo mass, large-scale mass density (measured over a few Mpc), and local mass density (measured within the N th neighbour). The spatially resolved IFS stellar kinematics provide robust measurements of the spin parameter λ_e and enable us to examine the relationship among λ_e , M_* , and galaxy environment. We find a strong correlation between λ_e and M_* , where the average λ_e decreases from ~ 0.4 to below 0.1 with increasing mass, and the fraction of slow rotators f_{slow} increases from $\sim 10\%$ to 90%. We show for the first time that at fixed M_* , there are almost no trends between galaxy spin and environment; the apparent kinematic morphology-density relation for ETGs is therefore primarily driven by M_* and is accounted for by the joint correlations between M_* and spin, and between M_* and environment. A possible exception is that the increased f_{slow} at high local density is slightly more than expected based only on these joint correlations. Our results suggest that the physical processes responsible for building up the present-day stellar masses of massive galaxies are also very efficient at reducing their spin, in any environment.

Key words: galaxies: elliptical and lenticular, cD – galaxies: evolution – galaxies: formation – galaxies: kinematics and dynamics – galaxies: structure

1 INTRODUCTION

As a group, elliptical galaxies obey the fundamental plane and have predominantly old stellar populations (e.g. Dressler et al. 1987; Djorgovski & Davis 1987; Baldry et al. 2004; Thomas et al. 2005). The properties of elliptical galaxies

vary considerably with mass, however, and can be grouped into two general families. Lower-mass elliptical galaxies have flattened isophotes, power-law central light profiles, and some net rotation that aligns with their shortest axis. More massive elliptical galaxies, in contrast, show boxy isophotes, cored light profiles, and small net rotation (e.g., Illingworth 1977; Davies et al. 1987; Bender et al. 1989; Kormendy & Bender 1996; Kormendy et al. 2009). The standard interpretation of these differences is that massive elliptical galax-

★ E-mail: melanie.veale@berkeley.edu (MV), cpma@berkeley.edu (C-PM)

ies experience a large number of relatively gas-free mergers that effectively erase any record of their spin, while at lower mass gas accretion and gas-rich mergers tend to preserve a net spin to the galaxies (e.g. Hoffman et al. 2010; Bois et al. 2011; Moody et al. 2014; Khochfar et al. 2011; Martizzi et al. 2014; Naab et al. 2014; Choi & Yi 2017; Penoyre et al. 2017). Stellar mass strongly determines whether a galaxy is a fast or slow rotator (e.g. Emsellem et al. 2011; Cappellari 2013; Veale et al. 2017). However, given that the merger and accretion history of a galaxy is partially determined by its surrounding large-scale environment, it is also important to assess the impact of galaxy environment on galaxy rotation.

Motivated by the classic morphology-density relation of Dressler (1980), a number of papers have investigated an analogous *kinematic* morphology-density relation using integral field spectrograph (IFS) data, comparing how late-type galaxies (LTGs), fast rotating early-type galaxies (ETGs), and slow rotating ETGs populate different density environments. Cappellari et al. (2011b) find that substituting kinematic morphology (i.e. fast or slow rotator status) for Hubble type (lenticular versus elliptical) yields a cleaner relationship than the traditional morphology-density relation. While a significant fraction of elliptical galaxies populate low-density environments, they find that nearly all of them are fast rotators more similar to inclined lenticular galaxies than to genuine spheroidal ellipticals. They also find that the fraction of slow rotators within the ETG population (excluding LTGs) increased at the highest local densities.

A handful of subsequent studies based on individual clusters also report an increased fraction of slow rotators in dense cluster centres (D'Eugenio et al. 2013; Houghton et al. 2013; Scott et al. 2014; Fogarty et al. 2014). However, although the fraction of slow rotators was higher in each cluster centre than in the outskirts, the overall fraction of slow rotators in each cluster did not depend on the size of the cluster or on the large-scale density of the cluster's environment. Jimmy et al. (2013) searched for signs of recent merging in several brightest cluster galaxies and companions, and find no particular connection between merging signatures and galaxy rotation. Recently, Oliva-Altamirano et al. (2017) find only a tentative increase in the fraction of slow rotators with cluster mass for central galaxies.

Most existing studies to date have been limited to a small number of rich environments, or a small volume probing the field. It is difficult, using these data sets, to decouple the correlated impact of stellar mass and environment on the demographics of slow and fast rotators. In order to control for stellar mass when investigating the importance of environment, it is necessary to span a full range of environments at the highest masses.

We designed the volume-limited MASSIVE survey to investigate systematically the most massive galaxies in the northern sky within a distance of 108 Mpc (Ma et al. 2014), targeting 116 galaxies with $M_K \lesssim -25.3$ mag ($M_* \gtrsim 10^{11.5} M_\odot$). This volume is large enough to sample a wide range of environments including several galaxy clusters, many galaxy groups, and galaxies in the field. The sample is thus complementary to the ATLAS^{3D} survey, which includes about twice as many galaxies but from a volume about ten times smaller; it is dominated by the Virgo cluster, and contains only six galaxies more massive than $10^{11.5} M_\odot$. Details

of the kinematic analysis of our IFS data were presented in Veale et al. (2017), which focused on the brightest 41 galaxies ($M_K < -25.7$ mag) in the MASSIVE survey. We have since completed observations and analysis of the larger sample of 75 galaxies with a limiting magnitude of $M_K = -25.5$ mag.

In this paper we perform a detailed analysis of the environments of the entire MASSIVE sample and present measurements of the spin of the 75 MASSIVE galaxies with Mitchell/VIRUS-P IFS data. Together with the ATLAS^{3D} sample of ETGs at lower masses, we investigate the influence of galaxy mass and environment on the spin of ETGs over a wide range of stellar mass ($8 \times 10^9 \lesssim M_* \lesssim 2 \times 10^{12} M_\odot$) and environment. In particular, the combined MASSIVE and ATLAS^{3D} sample from the two volume-limited IFS surveys has well-defined stellar mass selection and is large enough for us to conduct the first analysis of the relationship between spin and environment at fixed M_* for present-day ETGs, and assess how much of the kinematic morphology-density relation is driven by stellar mass.

Since different methods for quantifying environment probe different physical scales, we compare four approaches in this paper: (1) group membership, i.e., if a galaxy is the brightest galaxy or a satellite in a group/cluster, or is relatively isolated; (2) halo mass; (3) smoothed large-scale galaxy density field; and (4) local galaxy density based on the N th nearest neighbour. The fact that these measures cover differing length scale implies that they may correlate differently with quantities such as galaxy merger rates, assembly histories, and masses.

Section 2 of this paper summarizes the selection and properties of MASSIVE survey galaxies and ATLAS^{3D} galaxies. Section 3 presents results for the individual measurements and the statistics of the four environmental quantities. Technical details of our local density calculation are in Appendix A. Section 4 summarizes the kinematic analysis of our IFS data and presents results for galaxy spin versus stellar mass. Section 5 connects spin to environment, and explores how to decouple those trends from the influence of stellar mass. Section 6 discusses implications and conclusions. Details of the error bars we use to determine whether any trends are significant are presented in Appendix B. An application of our analysis to the original ATLAS^{3D} sample densities is presented in Appendix C. We assume $h = 0.7$ throughout the paper.

2 GALAXY SAMPLES

The MASSIVE survey consists of a volume-limited sample of early-type galaxies, targeting all 116 galaxies¹ with K -band magnitudes M_K brighter than -25.3 mag (i.e. stellar masses $M_* \gtrsim 10^{11.5} M_\odot$) and distances within $D < 108$ Mpc, in the northern hemisphere and away from the galactic plane (Ma et al. 2014). The galaxies were selected from the Extended Source Catalogue (XSC; Jarrett et al. 2000) of the Two Micron All Sky Survey (2MASS; Skrutskie et al.

¹ The actual count is 115 galaxies after we remove NGC 7681, as discussed in Veale et al. (2017), which our data showed to be a close pair of bulges. We likewise exclude NGC 7681 from this paper.

Table 1. Properties of MASSIVE survey galaxies

Galaxy	R.A.	Dec.	D	M_K	$\log_{10} M_*$	ε	λ_e	Rot.	env	$\log_{10} M_{\text{halo}}$	Cluster	$(1 + \delta_g)$	v_{10}
(1)	[deg]	[deg]	[Mpc]	[mag]	$[M_\odot]$	(7)	(8)	(9)	(10)	$[M_\odot]$	(12)	(13)	$[\bar{v}]$
(1)	(2)	(3)	(4)	(5)	(6)	(7)	(8)	(9)	(10)	(11)	(12)	(13)	(14)
NGC 0057	3.8787	17.3284	76.3	-25.75	11.79	0.17	0.02	S	I			2.3	4.9
NGC 0080	5.2952	22.3572	81.9	-25.66	11.75	0.09	0.04	S	B	14.1		3.0	6600
NGC 0128	7.3128	2.8641	59.3	-25.35	11.61	0.59			I			1.4	7.8
NGC 0227	10.6534	-1.5288	75.9	-25.32	11.60	0.25			B	13.5		4.0	4.6
NGC 0315	14.4538	30.3524	70.3	-26.30	12.03	0.28	0.06	S	B	13.5		6.0	280
NGC 0383	16.8540	32.4126	71.3	-25.81	11.82	0.14	0.25	F	S	14.4		7.2	4400
NGC 0393	17.1540	39.6443	85.7	-25.44	11.65	0.18*			I			1.5	1.4
NGC 0410	17.7453	33.1520	71.3	-25.90	11.86	0.25	0.03	S	B	14.4		7.4	3200
NGC 0467	19.7922	3.3008	75.8	-25.40	11.64	0.05			I			3.9	18
PGC 004829	20.1287	50.1445	99.0	-25.30	11.59	0.34*			I			2.6	10
NGC 0499	20.7978	33.4601	69.8	-25.50	11.68	0.35	0.06	S	S	14.4		7.2	36000
NGC 0507	20.9164	33.2561	69.8	-25.93	11.87	0.09	0.05	S	B	14.4		7.2	59000
NGC 0533	21.3808	1.7590	77.9	-26.05	11.92	0.26	0.03	S	B	13.5		4.3	13
NGC 0545	21.4963	-1.3402	74.0	-25.83	11.83	0.28	0.13	S	B	14.5	A194	5.9	14000
NGC 0547	21.5024	-1.3451	74.0	-25.83	11.83	0.14	0.06	S	S	14.5	A194	5.9	14000
NGC 0665	26.2338	10.4230	74.6	-25.51	11.68	0.24	0.40	F	B	13.7		3.0	58
UGC 01332	28.0755	48.0878	99.2	-25.57	11.71	0.30*	0.04	S	B	13.8		3.7	170
NGC 0708	28.1937	36.1518	69.0	-25.65	11.75	0.40*	0.04	S	B	14.5	A262	5.8	12000
UGC 01389	28.8778	47.9550	99.2	-25.41	11.64	0.34*			S	13.8		3.8	150
NGC 0741	29.0874	5.6289	73.9	-26.06	11.93	0.17	0.04	S	B	13.8		2.9	130
NGC 0777	30.0622	31.4294	72.2	-25.94	11.87	0.17	0.05	S	B	13.5		5.0	78
NGC 0890	35.5042	33.2661	55.6	-25.50	11.68	0.38*	0.10	S	I			4.7	1.4
NGC 0910	36.3616	41.8243	79.8	-25.33	11.61	0.16*			S	14.8	A347	6.2	12000
NGC 0997	39.3103	7.3056	90.4	-25.40	11.64	0.13			B	13.0		3.0	26
NGC 1016	39.5815	2.1193	95.2	-26.33	12.05	0.06	0.03	S	B	13.9		4.8	56
NGC 1060	40.8127	32.4250	67.4	-26.00	11.90	0.24	0.02	S	B	14.0		3.9	2100
NGC 1066	40.9579	32.4749	67.4	-25.31	11.60	0.16			S	14.0		3.9	2200
NGC 1132	43.2159	-1.2747	97.6	-25.70	11.77	0.37	0.06	S	B	13.6		3.4	8.3
NGC 1129	43.6141	41.5796	73.9	-26.14	11.96	0.15 [†]	0.12	S	B	14.8		10.7	16000
NGC 1167	45.4265	35.2056	70.2	-25.64	11.74	0.17	0.43	F	B	13.1		5.0	15
NGC 1226	47.7723	35.3868	85.7	-25.51	11.68	0.18*	0.03	S	B	13.2		3.5	3.1
IC0 310	49.1792	41.3248	77.5	-25.35	11.61	0.06			S	14.8	Perseus	13.2	15000
NGC 1272	49.8387	41.4906	77.5	-25.80	11.81	0.07	0.02	S	S	14.8	Perseus	13.5	400000
UGC 02783	53.5766	39.3568	85.8	-25.44	11.65	0.11			B	12.6		6.3	17
NGC 1453	56.6136	-3.9688	56.4	-25.67	11.75	0.14*	0.20	F	B	13.9		2.3	89
NGC 1497	60.5283	23.1329	87.8	-25.31	11.60	0.40*			I			2.7	89
NGC 1600	67.9161	-5.0861	63.8	-25.99	11.90	0.26*	0.03	S	B	14.2		6.0	1200
NGC 1573	68.7666	73.2624	65.0	-25.55	11.70	0.34*	0.04	S	B	14.1		4.1	590
NGC 1684	73.1298	-3.1061	63.5	-25.34	11.61	0.24*			B	13.7		6.2	1600
NGC 1700	74.2347	-4.8658	54.4	-25.60	11.72	0.28*	0.20	F	B	12.7		3.5	23
NGC 2208	95.6444	51.9095	84.1	-25.63	11.74	0.32*	0.06	S	I			2.8	7.2
NGC 2256	101.8082	74.2365	79.4	-25.87	11.84	0.20*	0.02	S	B	13.7		2.7	21
NGC 2274	101.8224	33.5672	73.8	-25.69	11.76	0.10*	0.07	S	B	13.3		3.1	110
NGC 2258	101.9425	74.4818	59.0	-25.66	11.75	0.24*	0.04	S	B	12.2		3.8	9.8
NGC 2320	106.4251	50.5811	89.4	-25.93	11.87	0.30*	0.23	F	B	14.2		7.9	660
UGC 03683	107.0582	46.1159	85.1	-25.52	11.69	0.26*	0.09	S	B	13.6		5.8	27
NGC 2332	107.3924	50.1823	89.4	-25.39	11.63	0.34*			S	14.2		7.8	1500
NGC 2340	107.7950	50.1747	89.4	-25.90	11.86	0.44*	0.03	S	S	14.2		7.8	1300
UGC 03894	113.2695	65.0791	97.2	-25.58	11.72	0.10	0.12	F	B	13.7		1.5	1.5
NGC 2418	114.1563	17.8839	74.1	-25.42	11.64	0.20			I			2.2	1.4
NGC 2456	118.5444	55.4953	107.3	-25.33	11.61	0.24*			I			2.4	3.7
NGC 2492	119.8738	27.0264	97.8	-25.36	11.62	0.19			B	13.0		1.1	0.8
NGC 2513	120.6028	9.4136	70.8	-25.52	11.69	0.20	0.10	S	B	13.6		2.3	5.2
NGC 2672	132.3412	19.0750	61.5	-25.60	11.72	0.14	0.10	S	B	13.0		1.3	1.3
NGC 2693	134.2469	51.3474	74.4	-25.76	11.79	0.25	0.29	F	I			1.7	6.9
NGC 2783	138.4145	29.9929	101.4	-25.72	11.78	0.39	0.04	S	B	12.8		3.2	4.7
NGC 2832	139.9453	33.7498	105.2	-26.42	12.08	0.31	0.07	S	B	13.7	A779	4.0	7.9
NGC 2892	143.2205	67.6174	101.1	-25.70	11.77	0.06	0.05	S	I			2.2	2.3
NGC 2918	143.9334	31.7054	102.3	-25.49	11.68	0.17			I			3.0	2.5
NGC 3158	153.4605	38.7649	103.4	-26.28	12.02	0.18	0.26	F	B	13.3		2.7	9.8
NGC 3209	155.1601	25.5050	94.6	-25.55	11.70	0.27	0.04	S	B	11.8		2.4	2.8
NGC 3332	160.1182	9.1825	89.1	-25.38	11.63	0.16			I			1.0	0.6

Table 1 – *continued*

Galaxy	R.A.	Dec.	D	M_K	$\log_{10} M_*$	ε	λ_e	Rot.	env	$\log_{10} M_{\text{halo}}$	Cluster	$(1 + \delta_g)$	ν_{10}
(1)	[deg]	[deg]	[Mpc]	[mag]	$[M_{\odot}]$	(7)	(8)	(9)	(10)	$[M_{\odot}]$	(12)	(13)	$[\bar{\nu}]$
NGC 3343	161.5432	73.3531	93.8	-25.33	11.61	0.32*			I			2.0	16
NGC 3462	163.8378	7.6967	99.2	-25.62	11.73	0.26	0.09	S	I			2.2	2.5
NGC 3562	168.2445	72.8793	101.0	-25.65	11.75	0.16*	0.04	S	B	13.5		2.2	8.5
NGC 3615	169.5277	23.3973	101.2	-25.58	11.72	0.38	0.40	F	B	13.6		3.1	5.2
NGC 3805	175.1736	20.3430	99.4	-25.69	11.76	0.36	0.50	F	S	14.8	A1367	5.6	440
NGC 3816	175.4502	20.1036	99.4	-25.40	11.64	0.31		S	S	14.8	A1367	5.8	1900
NGC 3842	176.0090	19.9498	99.4	-25.91	11.86	0.22	0.04	S	B	14.8	A1367	5.9	19000
NGC 3862	176.2708	19.6063	99.4	-25.50	11.68	0.06	0.06	S	S	14.8	A1367	5.9	18000
NGC 3937	178.1776	20.6313	101.2	-25.62	11.73	0.20	0.07	S	B	14.2		5.9	71
NGC 4055	181.0059	20.2323	107.2	-25.40	11.64	0.18			S	14.3		7.1	2300
NGC 4065	181.0257	20.2351	107.2	-25.47	11.67	0.22			B	14.3		7.1	2500
NGC 4066	181.0392	20.3479	107.2	-25.35	11.61	0.06			S	14.3		7.1	4200
NGC 4059	181.0471	20.4098	107.2	-25.41	11.64	0.06			S	14.3		7.1	4900
NGC 4073	181.1128	1.8960	91.5	-26.33	12.05	0.32	0.02	S	B	13.9		4.4	89
NGC 4213	183.9064	23.9819	101.6	-25.44	11.65	0.17			B	13.4		4.7	16
NGC 4472	187.4450	8.0004	16.7	-25.72	11.78	0.17 [†]	0.20	F	B	14.7	Virgo	8.9	1900
NGC 4486	187.7059	12.3911	16.7	-25.31	11.60	0.10			S	14.7	Virgo	9.1	14000
NGC 4555	188.9216	26.5230	103.6	-25.92	11.86	0.20	0.12	S	I			5.9	6.3
NGC 4649	190.9167	11.5526	16.5	-25.36	11.62	0.20			S	14.7	Virgo	9.1	2600
NGC 4816	194.0506	27.7455	102.0	-25.33	11.61	0.20			S	15.3	Coma	13.2	1900
NGC 4839	194.3515	27.4977	102.0	-25.85	11.83	0.35	0.05	S	S	15.3	Coma	13.2	2600
NGC 4874	194.8988	27.9594	102.0	-26.18	11.98	0.09	0.07	S	S	15.3	Coma	13.2	24000
NGC 4889	195.0338	27.9770	102.0	-26.64	12.18	0.36	0.03	S	B	15.3	Coma	13.2	19000
NGC 4914	195.1789	37.3153	74.5	-25.72	11.78	0.39	0.05	S	I			1.1	1.2
NGC 5129	201.0417	13.9765	107.5	-25.92	11.86	0.37	0.40	F	I			4.3	4.9
NGC 5208	203.1163	7.3166	105.0	-25.61	11.73	0.63	0.61	F	B	13.0		5.0	16
PGC 047776	203.4770	3.2836	103.8	-25.36	11.62	0.18			B	14.1		4.0	17
NGC 5252	204.5661	4.5426	103.8	-25.32	11.60	0.52			S	14.1		4.9	52
NGC 5322	207.3133	60.1904	34.2	-25.51	11.68	0.33	0.05	S	B	13.7		2.5	21
NGC 5353	208.3613	40.2831	41.1	-25.45	11.66	0.56			B	13.6		2.6	63
NGC 5490	212.4888	17.5455	78.6	-25.57	11.71	0.20	0.14	S	I			2.1	9.8
NGC 5557	214.6071	36.4936	51.0	-25.46	11.66	0.17			B	13.3		2.6	8.5
IC1 143	232.7345	82.4558	97.3	-25.45	11.66	0.14*			B	13.0		2.0	13
UGC 10097	238.9303	47.8673	91.5	-25.43	11.65	0.23			B	12.7		1.5	5.0
NGC 6223	250.7679	61.5789	86.7	-25.59	11.72	0.20*	0.32	F	B	13.5		1.5	6.2
NGC 6364	261.1139	29.3902	105.3	-25.38	11.63	0.15			I			0.8	0.5
NGC 6375	262.3411	16.2067	95.8	-25.53	11.69	0.10*	0.24	F	I			1.2	1.5
UGC 10918	264.3892	11.1217	100.2	-25.75	11.79	0.14*	0.03	S	I			1.8	4.8
NGC 6442	266.7139	20.7611	98.0	-25.40	11.64	0.12*			I			1.1	3.0
NGC 6482	267.9534	23.0719	61.4	-25.60	11.72	0.36*	0.14	S	B	13.1		1.6	1.1
NGC 6575	272.7395	31.1162	106.0	-25.58	11.72	0.28*	0.12	S	I			2.1	5.0
NGC 7052	319.6377	26.4469	69.3	-25.67	11.75	0.50*	0.15	S	I			1.3	0.8
NGC 7242	333.9146	37.2987	84.4	-26.34	12.05	0.28*	0.04	S	B	14.0		6.3	2800
NGC 7265	335.6145	36.2098	82.8	-25.93	11.87	0.22*	0.04	S	B	14.7		6.9	5200
NGC 7274	336.0462	36.1259	82.8	-25.39	11.63	0.06*			S	14.7		6.9	3200
NGC 7386	342.5089	11.6987	99.1	-25.58	11.72	0.28	0.07	S	B	13.9		2.6	3.2
NGC 7426	344.0119	36.3614	80.0	-25.74	11.79	0.34*	0.56	F	B	13.8		3.8	8.5
NGC 7436	344.4897	26.1500	106.6	-26.16	11.97	0.12	0.09	S	B	14.4		4.1	100
NGC 7550	348.8170	18.9614	72.7	-25.43	11.65	0.07			B	11.9		0.9	1.0
NGC 7556	348.9353	-2.3815	103.0	-25.83	11.83	0.25	0.05	S	B	14.0		2.0	17
NGC 7618	349.9468	42.8526	76.3	-25.44	11.65	0.28*			B	13.7		3.2	250
NGC 7619	350.0605	8.2063	54.0	-25.65	11.75	0.23	0.12	S	B	14.0		1.5	22
NGC 7626	350.1772	8.2170	54.0	-25.65	11.75	0.14	0.03	S	S	14.0		1.5	21

Column notes: (1) Galaxy name (in order of increasing right ascension). (2), (3) Right Ascension, Declination in degrees. (4) Distance according to [Ma et al. \(2014\)](#). (5) Extinction-corrected total absolute K -band magnitude. (6) Stellar mass estimated from M_K . (7) Ellipticity from NSA where available, from 2MASS otherwise (asterisks). [†] NGC 1129 and NGC 4472 are from our CFHT data and [Emsellem et al. \(2011\)](#) respectively; see [Veale et al. \(2017\)](#) for details. (8) Proxy for the spin parameter within the effective radius. (9) Slow or fast rotator classification. Most galaxies are slow rotators (“S”), with few fast rotators (“F”). See [Section 4.1](#) for definitions. (10) Group membership according to the HDC catalogue. Most galaxies are BGG (“B”), with few satellite (“S”) or isolated (“I”) galaxies. (11) Halo mass according to the HDC catalogue, or from updated literature sources (see text) for Virgo, Coma, and Perseus. (12) Membership in Virgo, Coma, Perseus, or Abell clusters. (13) Large-scale galaxy overdensity from the 2M++ catalogue ([Section 3.3](#)). (14) Local density in units of the mean K -band luminosity density $\bar{\nu} \sim 2.8 \times 10^8 L_{\odot} \text{Mpc}^{-3}$ ([Section 3.4](#)).

2006). Distances are taken from the surface-brightness fluctuation method (Blakeslee et al. 2009, 2010; Blakeslee 2013) for galaxies in Virgo and Coma, from the High Density Contrast (HDC) group catalogue (Crook et al. 2007, see also Section 3.1) for other galaxies if available, and from the flow model of Mould et al. (2000) otherwise. We use M_K as a proxy for the stellar mass, estimated using equation 2 of Ma et al. (2014). That equation was taken from equation 2 of Cappellari (2013), a fit to stellar masses derived from dynamical modeling.

We have completed observations of the ‘‘priority sample’’ of the MASSIVE survey, which consists of the 75 galaxies with $M_K < -25.5$ mag ($M_* \gtrsim 10^{11.7} M_\odot$). The observations were performed using the Mitchell/VIRUS-P IFS at the McDonald Observatory (Hill et al. 2008), which has a large $107'' \times 107''$ field of view and consists of 246 evenly-spaced $4''$ -diameter fibres with a one-third filling factor. We observed each galaxy with three dither positions of equal exposure time to obtain contiguous coverage of the field of view. The spectral range spanned 3650 \AA to 5850 \AA , covering the Ca H+K region, the G-band region, H β , the Mg β region, and many Fe absorption features, with ~ 2000 pixels (log-spaced in wavelength) and an instrumental resolution of $\sim 4.5 \text{ \AA}$ full width at half-maximum.

We spatially bin our IFS spectra to obtain a mean signal-to-noise ratio (S/N) of at least 20 (per pixel) for each spectrum, folding across the major axis to combine symmetrical bins and obtain our minimum S/N with the smallest possible bin size. To obtain the stellar line-of-sight velocity distribution (LOSVD) for each spectrum, we use the penalized pixel-fitting (pPXF) method of Cappellari & Emsellem (2004) and parametrize the LOSVD as a Gauss-Hermite series up to order 6. For each spectrum we thus obtain velocity V , dispersion σ , and higher order moments h_3, h_4, h_5 and h_6 . See Veale et al. (2017) for a more detailed description of the analysis.

There are two main sources of uncertainty on M_K . First, the K -band magnitudes of 2MASS are likely underestimated somewhat due to the shallowness of the survey (Lauer et al. 2007; Schombert & Smith 2012). Second, the choice of distance estimate and extinction (see Ma et al. 2014 for details) can also impact M_K and M_* ; based on the galaxies in common between MASSIVE and ATLAS^{3D}, typical differences in M_K due to different estimates is around 0.1 mag, and up to nearly 0.5 mag for extreme cases. These are both larger than the uncertainty due to formal errors in K -band magnitude from 2MASS, which are generally less than 0.03 mag. Together, combined with the 0.14 dex scatter in the M_* - M_K relation (Cappellari 2013), these correspond to an underestimation of M_* of up to ~ 0.3 dex, and an uncertainty of ~ 0.2 dex.

Where available, additional photometric data is taken from the NASA-Sloan Atlas (NSA, <http://www.nsatlas.org>) based on the SDSS DR8 catalogue (York et al. 2000; Aihara et al. 2011); otherwise the 2MASS values are used. The effective radius R_e from these sources, like M_K , may be underestimated due to the shallowness of the surveys. We have scaled the 2MASS R_e to be comparable to the NSA values (see Ma et al. 2014, for details) to partly account for the 2MASS underestimation. Comparing ellipticity ε and position angle (PA) of galaxies with both NSA and 2MASS data gives an estimate of uncertainties in those quantities

of ~ 0.05 and ~ 15 degrees, respectively. Very round galaxies may have much higher uncertainties in PA; we discuss in Section 4.1 how this impacts our kinematic analysis, and why we do not expect these uncertainties (or the underestimation of R_e) to impact our results. Results from our deep CFHT photometry will be reported in upcoming MASSIVE papers.

As a comparison sample to MASSIVE, we examine the 260 nearby galaxies in the ATLAS^{3D} survey (also selected from the 2MASS XSC), which targets all early-type galaxies with $M_K < -21.5$ mag ($M_* \gtrsim 10^{9.9} M_\odot$) and located within $D < 42$ Mpc, also in the northern hemisphere and excluding the galactic plane (Cappellari et al. 2011a). Due to the larger volume and brighter M_K cutoff of the MASSIVE survey, only 6 ATLAS^{3D} galaxies overlap with MASSIVE. The two surveys therefore target complementary parameter space in stellar mass and volume. Of the 6 common galaxies, NGC 4472 and NGC 5322 are in the priority sample ($M_K < -25.5$ mag) presented in this paper, while the remaining 4 (NGC 4486, 4649, 5353, 5557) are fainter than this limit. Our kinematic measurements of V , σ , h_3 and h_4 agree well with ATLAS^{3D} for the inner $\sim 25''$ region of each galaxy covered by ATLAS^{3D}, but our data extend to at least $\sim 60''$ in radius (see Figure B1 of Veale et al. 2017, where we compare kinematics from both surveys for NGC 4472, 5322, and 5557). We use our wide-field kinematic results for NGC 4472 and NGC 5322 below and remove these two galaxies from the ATLAS^{3D} sample in our plots, to avoid double-counting and create a clean separation in M_K between the two samples.

We note that $\sim 20\%$ of galaxies in the ATLAS^{3D} sample are in the Virgo cluster. These galaxies are powerful probes of the intra-cluster environments within Virgo, but they probe only a single cluster. By contrast, no MASSIVE galaxy resides in a galaxy group or cluster (as defined in Section 3.1) containing more than three other MASSIVE galaxies. The MASSIVE sample therefore tends to probe distinct group/cluster environments. When appropriate, we will denote Virgo galaxies in the ATLAS^{3D} sample with distinct symbols below so that the rest of ATLAS^{3D} sample can be compared with the MASSIVE sample more fairly.

3 GALAXY ENVIRONMENTS

In this paper we use four different measures to quantify galaxy environments and to investigate the connection between galaxy environments and stellar kinematics for the galaxies in the MASSIVE and ATLAS^{3D} surveys: (1) group membership from the group catalogues of Crook et al. (2007) constructed from the 2MASS Redshift Survey (2MRS; Huchra et al. 2012); (2) halo mass from the same group catalogues, available for galaxies in a group with 3 or more members; (3) a smoothed large-scale density field from Carrick et al. (2015) based on the 2M++ Redshift Catalogue of Lavaux & Hudson (2011); and (4) a local galaxy luminosity density calculated within the volume to the 10th neighbour, similar to ν_{10} in Cappellari et al. (2011b). We discuss the differences and caveats of the four methods in the subsections below. See also, e.g., Muldrew et al. (2012) for a comprehensive study of different definitions of galaxy environments, and Carollo et al. (2013) for a discussion of

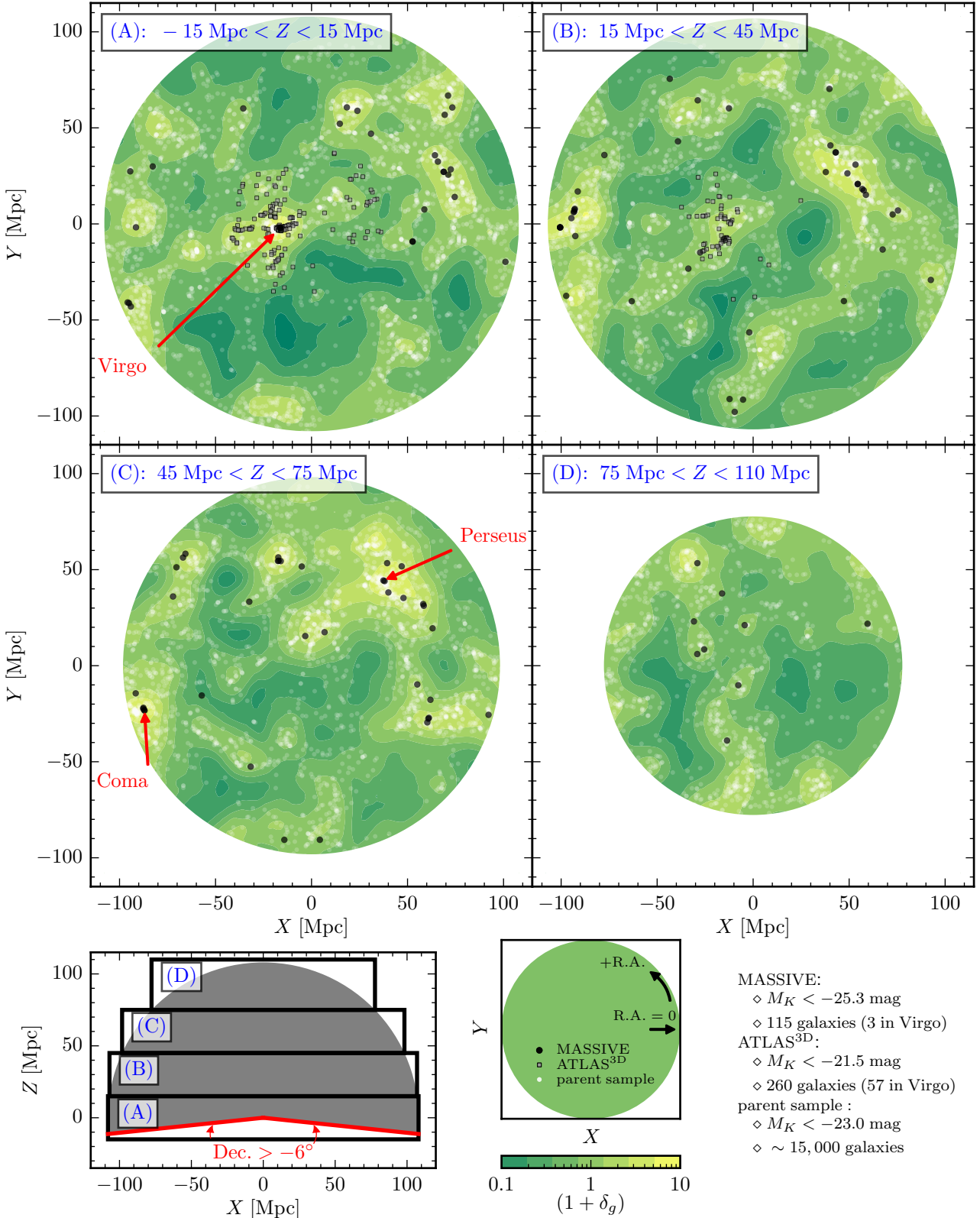


Figure 1. Galaxy distribution in the MASSIVE survey volume, where the X - Y plane is the earth equatorial plane, in four vertical slices. Galaxies in the MASSIVE survey (black circles) span a volume more than 10 times that of the ATLAS^{3D} galaxies (grey squares). Contour map colours (yellow to dark green) show the large-scale density $(1 + \delta_g)$ from the 2M++ Redshift Catalogue, averaged over Z within the slice at each pixel. These contours trace closely the galaxy locations of the parent sample selected from 2MRS for purposes of calculating local density ν_{10} (see Appendix A for details) which are shown as transparent white points (areas of many overlapping galaxies are brighter). With a cut of $M_K < -23.0 \text{ mag}$, 2MRS (and hence our parent sample) is nearly complete out to our maximum distance of $D = 108 \text{ Mpc}$ (see Appendix A).

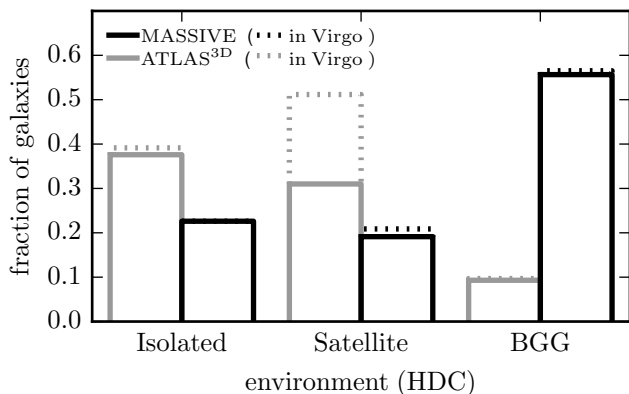


Figure 2. Distribution of MASSIVE (black) and ATLAS^{3D} (grey) galaxies in three environment types based on the 2MRS HDC group catalogue. The galaxy fractions are computed within each survey: 56% of MASSIVE galaxies are BGGs, whereas only 10% of ATLAS^{3D} galaxies are BGGs. Virgo galaxies (dotted lines) are stacked above non-Virgo galaxies. About 20% of ATLAS^{3D} satellite galaxies are in the Virgo cluster, and some Virgo galaxies are classified as isolated due to different definitions of the cluster boundaries between ATLAS^{3D} and the 2MRS HDC group catalogue. The small fraction of BGGs in ATLAS^{3D} is expected due to the inclusion of galaxies as faint as -21.5 mag, especially the many Virgo galaxies, but may be made even smaller by incompleteness in the HDC catalogue (see text).

how a similar set of environment measures connects to other galaxy properties such as size, color, and star formation rate. Each measure of environment is tabulated in Table 1. An overview of the MASSIVE volume is shown in Figure 1.

3.1 Group Membership

Crook et al. (2007, 2008) published redshift-limited catalogues of galaxy groups based on a 2MRS sample complete to an apparent magnitude (corrected for extinction) of $K < 11.25$ mag (Huchra et al. 2005a,b). This limiting magnitude corresponds to an absolute magnitude of approximately $M_K < -23.9$ mag at our maximum distance of 108 Mpc, and approximately $M_K < -21.9$ mag at the maximum ATLAS^{3D} distance of 42 Mpc. The group catalogues thus cover both MASSIVE ($M_K < -25.3$ mag) and ATLAS^{3D} galaxies ($M_K < -21.5$ mag), with only two ATLAS^{3D} galaxies (PGC 029321 and UGC 05408) falling outside the magnitude cut.

Crook et al. (2007) applied the Friends-of-Friends (FOF) algorithm with two sets of linking parameters to create two group catalogues of differing density contrasts. The High Density Contrast (HDC) catalogue used a linking length of 350 km s^{-1} along the line of sight and 0.89 Mpc in the transverse direction, corresponding to a density contrast of $\delta\rho/\rho \gtrsim 80$. The Low Density Contrast (LDC) catalogue used larger linking lengths of 399 km s^{-1} and 1.63 Mpc for a density contrast of $\delta\rho/\rho \gtrsim 12$. In Ma et al. (2014) we compared and discussed the agreement between the group assignments of the HDC and the 2M++ redshift catalogue of Lavaux & Hudson (2011).

We classify MASSIVE and ATLAS^{3D} galaxies into three types according to their group membership in the HDC cat-

alogue: (1) “brightest group galaxy” (BGG) that belongs to a group and is the most luminous galaxy in the group; (2) “satellite” that belongs to a group but is not the BGG; and (3) “isolated” galaxy that does not belong to a group of at least 3 members in the catalogue. We make no attempt to determine whether the BGG of a group is also the *central* galaxy of the group, which it may not be (e.g. Skibba et al. 2011); see Oliva-Altamirano et al. (2017) for a discussion of rotation in central galaxies.

Figure 2 shows that among the 116 MASSIVE galaxies, 56% are BGGs, 21% are satellites in groups, and 23% are “isolated”, whereas in ATLAS^{3D}, most of the galaxies are either satellites (51%) or isolated (39%), with only 10% being BGGs. The much lower percentage of BGGs in ATLAS^{3D} than MASSIVE is largely a result of the smaller survey volume and lower mass limit of the ATLAS^{3D} survey. It may also be further suppressed by the relative incompleteness of the HDC catalogue near the edges of the ATLAS^{3D} volume. While only two ATLAS^{3D} galaxies are outside the magnitude cut of Crook et al. (2007) entirely, group membership status also depends on whether nearby galaxies are inside or outside this cut. For example, the same galaxy might be classified as BGG of a group with 4 members at a close distance, but classified as isolated at a farther distance due to all 3 satellite galaxies falling outside the magnitude cut. Thus, ATLAS^{3D} galaxies near the edge of the sample and near the completeness limit of the Crook et al. (2007) catalogues may be biased towards classification as isolated.

In principle all MASSIVE galaxies beyond the ATLAS^{3D} volume are also subject to this relative bias towards being classified as isolated, but this will only occur if the (unidentified) rank 2 galaxy is below the $K = 11.25$ magnitude cut ($M_K = -23.9$ mag at $D = 108$ Mpc, compared to $M_K < -25.3$ for MASSIVE galaxies). Most groups have a smaller gap between BGG and rank 2 galaxies than this, so we proceed with the classifications as they are. We are consistent with high-redshift studies showing progenitors of our very massive galaxies in isolated environments (Vulcani et al. 2016).

We will use both HDC and LDC catalogues to provide group distances in Section 3.4 and Appendix A, instead of the improved distances calculated in Ma et al. (2014), for purposes of calculating local density ν_{10} ; see those sections for details.

3.2 Halo Mass

The group catalogues of Crook et al. (2007) also include dynamical estimates of dark matter halo masses for groups with at least 3 members. Two measurements of each halo are listed, one based on the standard virial estimator and the other based on the projected mass estimator (Heisler et al. 1985). We use the latter since the former is sensitive to close pairs and can be noisy for groups not uniformly sampled spatially (e.g. Bahcall & Tremaine 1981). Uncertainties on the projected mass estimator can be up to 0.5 dex for groups with only a few members, though they become smaller for groups with many members (Heisler et al. 1985).

For the MASSIVE galaxies, 89 are in groups with 3 or more members and have available M_{halo} from the HDC catalogue. For the 258 ATLAS^{3D} galaxies not observed with MASSIVE, 158 are in groups with M_{halo} measurements in

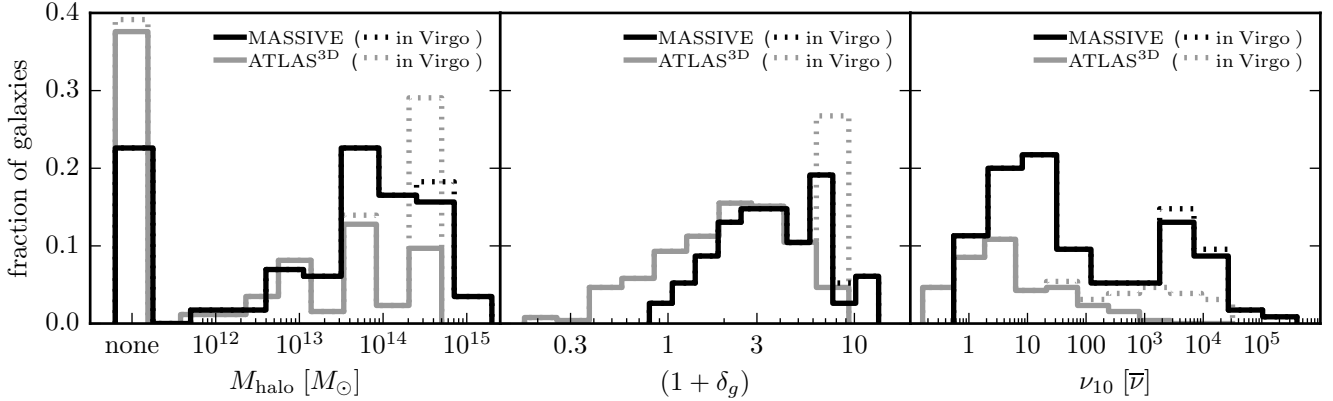


Figure 3. Distribution of MASSIVE (black) and ATLAS^{3D} galaxies (grey) in bins of halo mass M_{halo} (left panel), large scale density $(1 + \delta_g)$ (middle panel), and local density ν_{10} (right panel). Galaxies with fewer than 3 group members in the 2MRS HDC catalogue do not have M_{halo} measurements; these “isolated” galaxies are placed in the bin labeled “none” in the left panel. In each panel, Virgo galaxies (dotted lines) are stacked above non-Virgo galaxies. We use the ATLAS^{3D} definition of Virgo (within a sphere of $R = 3.5$ Mpc), but some “non-Virgo” galaxies are also in the same group as defined by the HDC catalogue, so less than half of the “non-Virgo” galaxies in the highest M_{halo} bin are actually in a different HDC group. All Virgo galaxies are found at close to the same δ_g , because the 5.7 Mpc smoothing scale of δ_g is larger than the 3.5 Mpc size of Virgo as defined for ATLAS^{3D} galaxies. The fractions of ATLAS^{3D} galaxies in each ν_{10} bin does not add up to 1, because our ν_{10} is calculated using a parent sample of $M_K < -23.0$ (see Appendix A for details).

the same catalogue. Additional halo mass measurements based on more detailed analyses are available for the three well-studied clusters of Virgo, Coma, and Perseus. For Virgo, we use $M_{\text{halo}} = 5.5 \times 10^{14} M_{\odot}$ (same as in Durrell et al. 2014), which is a combination of the Virgo A and B sub-cluster masses (Ferrarese et al. 2012) and the M86 sub-cluster mass (Schindler et al. 1999). For Coma, we use $M_{\text{halo}} = 1.8 \times 10^{15} M_{\odot}$, an average between $2.7 \times 10^{15} M_{\odot}$ (Kubo et al. 2007) from weak gravitational lensing measurements and $9.2 \times 10^{14} M_{\odot}$ (Falco et al. 2014, see also Rines et al. 2003) from galaxy dynamics. For Perseus, we use $M_{\text{halo}} = 6.7 \times 10^{14} M_{\odot}$ from spatially-resolved Suzaku X-ray observations (Simionescu et al. 2011).

The left panel of Figure 3 compares the distribution of M_{halo} in the two surveys. Nearly 40% of MASSIVE galaxies are in haloes above $10^{14} M_{\odot}$, whereas only $\sim 5\%$ of ATLAS^{3D} galaxies *outside* of the Virgo region are in such massive haloes. The leftmost bin shows “isolated” galaxies with fewer than 3 group members in the HDC catalogue and hence with no available M_{halo} measurements; a higher fraction of ATLAS^{3D} galaxies belong to this category than MASSIVE galaxies ($\sim 40\%$ versus 23% ; see also Section 3.1 and Figure 2).

3.3 Large-scale density

The group membership and group halo mass that we have investigated thus far provide information about galaxy environment on scales of a few hundred kpc to ~ 1 Mpc. Another useful measure of galaxy environment is the large-scale density field surrounding a galaxy on the scale of several Mpc. To this end, we use the density field of Carrick et al. (2015) constructed from the 2M++ redshift catalogue of Lavaux & Hudson (2011). The 2M++ catalogue contains 69,160 galaxy redshifts from 2MRS, the Sloan Digital Sky Survey Data Release 7 (SDSS-DR7; Abazajian et al. 2009), and the 6dF galaxy redshift survey Data Release 3 (6dFGRS-DR3; Jones

et al. 2009). It covers nearly the full sky and reaches a depth of $K = 12.5$ mag, deeper than $K = 11.75$ mag for the 44,599 galaxies in 2MRS alone.

Carrick et al. (2015) presents a luminosity-weighted galaxy density contrast, $\delta_g \equiv (\rho_g - \bar{\rho}_g)/\bar{\rho}_g$, smoothed with a 5.7 Mpc Gaussian kernel. This density field is computed with weights assigned to each galaxy’s luminosity to account for the magnitude limit of the survey and incompleteness. It is also rescaled to account for the impact of luminosity dependent galaxy-matter bias on the density field calculated at different redshifts. The result is a smoothed density field complete out to a distance of 178 Mpc (and partial coverage to a further distance of 286 Mpc). Our survey (out to 108 Mpc) is well within this radius.

The grid spacing of the published density field is approximately 2.2 Mpc. We compute the density at the location of each galaxy using a simple trilinear interpolation, which results in interpolation errors of approximately 0.1 dex. For galaxy distance, we use the LDC group-corrected distance where available, and redshift distances from Huchra et al. (2012) otherwise (assuming $h = 0.73$ as in Crook et al. 2007). We use these distances here instead of the distances from Ma et al. (2014) because they are more comparable to the reconstruction procedure in Carrick et al. (2015), but uncertainties in distance estimates will result in uncertainties in the density.

The middle panel of Figure 3 shows the distributions of δ_g for the entire MASSIVE versus ATLAS^{3D} sample. The values of δ_g for the 75 MASSIVE galaxies with stellar kinematics are listed in Table 1. While all MASSIVE galaxies are in regions above or near the cosmic mean density, about 20% of ATLAS^{3D} galaxies are in underdense or mean-density regions. The Coma cluster and Perseus cluster are the two highest-density regions sampled by the MASSIVE survey, both with $\delta_g \approx 12$. In comparison, the Virgo cluster is the highest-density region sampled by the ATLAS^{3D} survey with $\delta_g \approx 8$ (dotted line in Figure 3). Because δ_g is smoothed over

a scale larger than the size of a galaxy cluster, all galaxies in the same cluster have the same δ_g .

Figure 1 is a sky map of δ_g contours over the MASSIVE volume. The MASSIVE galaxies (black circles) are located in regions with $\delta_g \gtrsim 0$ (yellow and light green), whereas many ATLAS^{3D} galaxies (grey squares) are in the Virgo cluster or lower density regions (dark green). As expected, the parent sample of $\sim 15,000$ early-type galaxies with $M_K < -23.0$ mag from 2MRS (white dots) traces the δ_g contours quite well.

3.4 Local density

Finally, we calculate a local galaxy density by finding the distance to the N th nearest neighbour of a galaxy and estimating the luminosity (or mass) enclosed in this region. Several versions of local densities were tabulated in Cappellari et al. (2011b) for the ATLAS^{3D} sample. We will focus on ν_{10} , the luminosity density of galaxies in a sphere enclosing the 10th nearest neighbour (where the galaxy itself is counted as the 0th neighbour).

The galaxy sample used to estimate ν_{10} in Cappellari et al. (2011b) included all 2MRS galaxies (including spirals) with $M_K < -21.5$ mag in the ATLAS^{3D} volume. This cut matches the completeness limit $K = 11.75$ mag of 2MRS, which corresponds to $M_K \approx -21.5$ mag at the edge of the ATLAS^{3D} volume (42 Mpc). At the edge of the much larger volume probed by MASSIVE (108 Mpc), however, 2MRS is complete only to $M_K \approx -23.4$ mag. Using the same parent sample as in ATLAS^{3D} to calculate ν_{10} for MASSIVE galaxies would thus suffer substantially from incompleteness. Instead, we choose a magnitude cut of $M_K = -23.0$ mag for defining the parent 2MRS sample and compute ν_{10} from this sample of approximately 10^4 galaxies for both MASSIVE and ATLAS^{3D} galaxies, for a fair comparison between the two surveys. For simplicity and uniformity, we use HDC group distances (where available; LDC group distances otherwise, and redshift distances as a last resort) for all galaxies in this calculation. This includes the survey galaxies, even if they have more accurate distances tabulated in Ma et al. (2014) or Cappellari et al. (2011a). Using group distances results in typical uncertainties of about 0.5 dex on ν_{10} , due to individual galaxy distances being flattened to the group distance. Rarely, ν_{10} may be inflated by more than this because the distance flattening also re-orders the closest neighbors, but this impacts only a handful of galaxies. Additional details are discussed in Appendix A.

The distribution of the resulting ν_{10} for each survey is shown in the right panel of Figure 3. The values of ν_{10} for the MASSIVE priority sample are listed in Table 1. We express ν_{10} in units of the mean K -band luminosity density $\bar{\nu} \sim 2.8 \times 10^8 L_\odot \text{ Mpc}^{-3}$ for magnitude ranges of $-21 > M_K > -25$ mag from Table 2 of Lavaux & Hudson (2011). As their Table 2 shows, enlarging the range to $-17 > M_K > -25$ mag would raise $\bar{\nu}$ by only 5%, so the accuracy of the magnitude range is not a concern.

Figure 3 and Table 1 show that MASSIVE galaxies span about five orders of magnitude in ν_{10} , reaching ν_{10} above 10^4 for galaxies at the centres of the Coma cluster, Perseus cluster, Virgo cluster, Abell 194, Abell 262, Abell 347, and Abell 1367.

An alternate measure of local density is Σ_3 , defined as

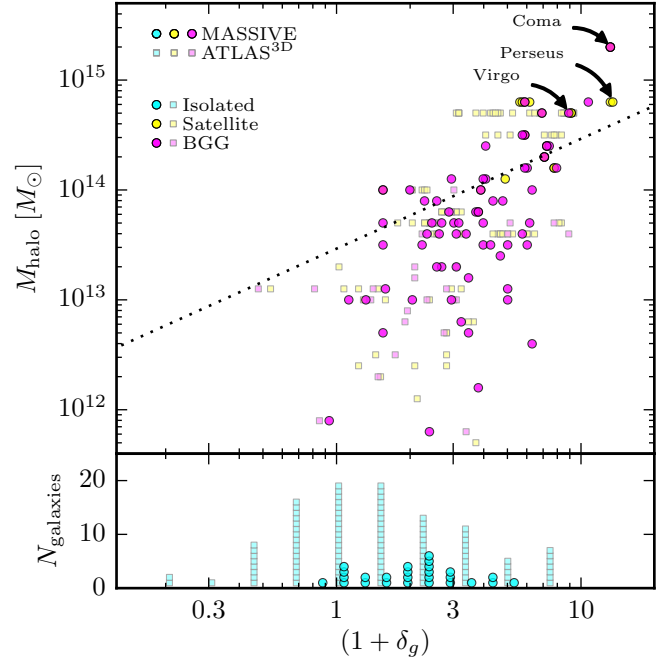


Figure 4. (Top) Halo mass M_{halo} versus large-scale density field $1 + \delta_g$ for MASSIVE (circles) and ATLAS^{3D} (squares) galaxies, where BGGs (magenta) and satellites (yellow) are colour-coded separately. Most satellite galaxies are hidden behind their respective BGGs since they have identical or very similar δ_g . The dotted line shows the extreme case when the halo mass dominates the total mass within the volume V of a sphere with radius of the smoothing distance (5.7 Mpc) used to measure δ_g , i.e., $M_{\text{halo}} = (1 + \delta)\bar{\rho}V$. Along this line, δ_g is simply measuring M_{halo} ; away from this line, δ_g and M_{halo} offer independent measures of a galaxy’s environment. (Bottom) Galaxies with fewer than 3 group members in the HDC catalogue are classified as isolated and have no estimated halo mass; the distribution of their δ_g are shown (cyan).

the number density of galaxies in a cylinder of 600 km s^{-1} in height, enclosing the 3 nearest neighbours, centred on the galaxy. This avoids the requirement of good redshift-independent distances by replacing it with a flat cutoff requiring neighbours to have heliocentric velocities within 300 km s^{-1} of the central galaxy. It is more sensitive to issues of survey completeness, and the overall results using Σ_3 are not much different than those using ν_{10} , so we do not discuss it in the body of the paper. For completeness, we do present results in Appendix C for the original Σ_3 and ν_{10} densities calculated in Cappellari et al. (2011a).

3.5 Relationships among different measures of environment

Here we examine how the environmental measures discussed above – group membership, M_{halo} , δ_g , and ν_{10} – correspond to one another. The distributions in δ_g for isolated galaxies in the two surveys are shown at the bottom of Figure 4. The top panel of Figure 4 shows M_{halo} vs δ_g for BGGs (magenta) and satellites (yellow), where higher-mass haloes generally reside in higher-density regions. This is expected since clusters of mass above $\sim 10^{14} M_\odot$ dominate the overden-

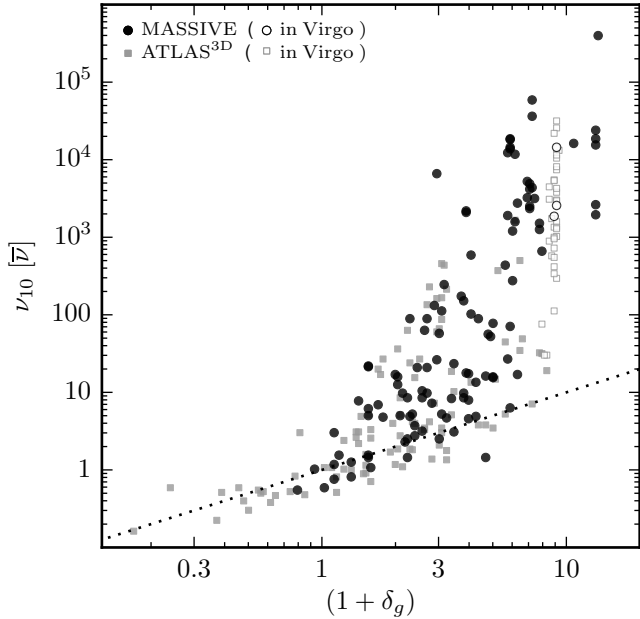


Figure 5. Local density ν_{10} versus large-scale density $1 + \delta_g$ for MASSIVE (black circles) and ATLAS^{3D} (grey squares) galaxies. At low densities, ν_{10} and $(1 + \delta_g)$ follow the dotted one-to-one line almost exactly, as expected when the 10th neighbour is at a distance comparable to the smoothing scale for δ_g . At high densities, e.g., within the Virgo cluster (open symbols), ν_{10} measures the local galaxy density and spans a much larger range than δ_g .

sity within 5.7 Mpc, the smoothing scale of δ_g . If a galaxy halo with M_{halo} were the only mass within the smoothing volume V (of radius 5.7 Mpc), the overdensity would be $M_{\text{halo}} = (1 + \delta)\bar{\rho}V$, as indicated by the dotted line in Figure 4. The galaxies with $M_{\text{halo}} \gtrsim 10^{14} M_{\odot}$ indeed lie near this line. Many lower-mass halos, on the other hand, lie to the right of this line since δ_g measures the large-scale density field rather than the halo mass itself in this regime; δ_g therefore spans a wide range of values, from near the cosmic mean to regions with δ_g near 10.

Satellite galaxies are sometimes visible as “tails” to the left of the BGG galaxy in the same halo in Figure 4, when the halo is large enough for the outskirts to show noticeably lower density on the smoothing scale of δ_g . Many more satellite galaxies, however, are hidden behind their BGG galaxies on this figure; in particular, all galaxies defined as Virgo galaxies by ATLAS^{3D} are within one symbol-width of the Virgo BGG. The other satellites defined as part of the same halo by the HDC catalogue were not designated as Virgo galaxies in ATLAS^{3D}.

Figure 5 shows the relationship between local density ν_{10} and large-scale density δ_g . At low densities, where both the distance to the 10th neighbour and the smoothing scale of δ_g are at scales beyond the size of the host halo, ν_{10} follows δ_g almost exactly. In dense regions, however, ν_{10} and δ_g can deviate significantly, where ν_{10} is determined by the innermost 10 galaxies well within a single host halo, while δ_g continues to measure the overdensity on several Mpc scale surrounding the galaxy. The Virgo galaxies (open symbols) illustrate this difference, showing a large spike in

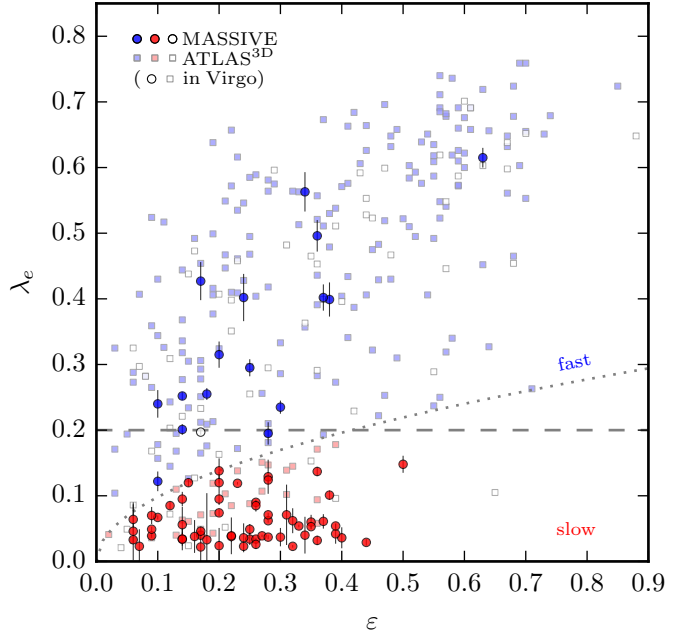


Figure 6. Spin parameter λ_e versus ellipticity ϵ for MASSIVE (circles) and ATLAS^{3D} (squares) galaxies. Open symbols indicate Virgo galaxies. Slow (red) and fast (blue) rotators can be separated by either a flat cutoff (dashed line; Lauer 2012), or one that takes into account ellipticity (dotted line; Emsellem et al. 2011). We use the latter cutoff in this analysis, but have tested that a flat cutoff does not qualitatively change the results.

ν_{10} relative to δ_g . Perseus shows the highest ν_{10} , and other groups/clusters (including Coma) in dense environments are similarly far above the smoothed density δ_g .

4 GALAXY SPIN VERSUS STELLAR MASS

In this section we present measurements of rotation in MASSIVE galaxies and investigate the dependence of galaxy spin on M_* and M_K in the ATLAS^{3D} and MASSIVE surveys. Here, and throughout the rest of the paper, we consider the 75 galaxies of the priority sample ($M_K < -25.5$ mag, $M_* \gtrsim 10^{11.7} M_{\odot}$) of the MASSIVE survey, for which we have completed the Mitchell IFS observations. This sample nearly doubles the 41 galaxies brighter than $M_K = -25.7$ mag reported in Veale et al. (2017).

4.1 Galaxy spin λ_e

As discussed in Section 2, our kinematic data provide measurements of the stellar velocity (V), dispersion (σ), and higher velocity moments (h_N) for each spatial bin folded across the major axis. We use the dimensionless parameter λ to quantify the relative importance of rotation in a galaxy:

$$\lambda(< R) \equiv \frac{\langle R|V| \rangle}{\langle R\sqrt{V^2 + \sigma^2} \rangle}, \quad \lambda_e \equiv \lambda(< R_e), \quad (1)$$

where the angle brackets represent luminosity-weighted averages over all bins within R (Emsellem et al. 2007). The

luminosity-weighting and cumulative nature of $\lambda(< R)$ prevents it from varying rapidly past R_e , unlike the local $\lambda(R)$ sometimes used to investigate radial gradients in rotation structure. The fact that our $\lambda(< R)$ is largely flat by R_e is important to minimize any bias in λ_e due to possibly underestimated R_e measurements (Veale et al. 2017).

The values of λ_e for the 75 MASSIVE galaxies are plotted against ellipticity in Figure 6 (circles) and are listed in Table 1. The ATLAS^{3D} sample is also shown (squares) for comparison. We note that our measurements of λ_e use circular bins (Veale et al. 2017), whereas ATLAS^{3D} uses elliptical apertures. Since most MASSIVE galaxies are quite round ($\varepsilon < 0.4$), the difference between circular and elliptical apertures is likely to be insignificant. Emsellem et al. (2011) classified galaxies as fast or slow rotators according to $\lambda_e = 0.31\sqrt{\varepsilon}$, where all galaxies with λ_e below this cutoff are defined as slow rotators. A flat cutoff at $\lambda_e = 0.2$ had also been suggested (Lauer 2012), and could be appropriate for our galaxies for several reasons as discussed in Veale et al. (2017). We have tested that the conclusions of this paper are not changed if we use this flat cutoff, which by extension ensures that our conclusions are not impacted by uncertain measurements of ε . For simplicity, we use only the ATLAS^{3D} cutoff hereafter.

We note that the IFS observations of many ATLAS^{3D} galaxies do not reach R_e , so their tabulated λ_e is calculated within a smaller radius than in the MASSIVE survey. About half of ATLAS^{3D} galaxies have data extending to between $0.5R_e$ and R_e , and about 8% have observations extending to less than $0.5R_e$ (Emsellem et al. 2011). Because many galaxies show a rising $\lambda(< R)$ profile within R_e , this may result in under-estimated λ_e for ATLAS^{3D} galaxies, and perhaps in fast rotators being misclassified as slow rotators. For a galaxy with $\lambda(< R)$ measured to $0.5R_e$, the appropriate slow/fast cutoff would be reduced by a factor of ~ 1.2 (Emsellem et al. 2011). Based on this rough scaling, only 4 ATLAS^{3D} galaxies may be misclassified as slow rotators. One of these is NGC 4472 (discussed in detail in Veale et al. 2017), which has $\lambda_e = 0.077$ according to Emsellem et al. (2011), measured with data going to only $0.26R_e$, and has $\lambda_e = 0.2$ in our sample. Of the remaining overlap galaxies between MASSIVE and ATLAS^{3D}, only NGC 5322 and NGC 5557 (below the $M_K < -25.5$ cut of this paper) have been observed, and they both agree to within about $\Delta\lambda_e \sim 0.02$ with the results of ATLAS^{3D}.

Another source of uncertainty is the measured PA of the galaxies; because we fold our data over the photometric PA, any misalignment between the rotation axis and photometric minor axis would wash out the rotation. NGC 1129 and NGC 4874 were misaligned in this way, so we manually adjusted the folding PA (see Veale et al. 2017). Based on those manual adjustments we estimate minor misalignments (~ 10 degrees) to reduce λ_e by ~ 0.01 , although the impact may be greater for faster rotators. Formal errors on λ_e , calculated from the uncertainties on V and σ in each bin according to the formulae in Houghton et al. (2013), are shown in Figure 6 for MASSIVE galaxies. They are generally smaller than the potential systematic uncertainties discussed here, with over half of MASSIVE galaxies having formal errors less than 0.01. Finally, the V and σ used to calculate λ_e may differ by up to 10% between Gaussian-only fits (as

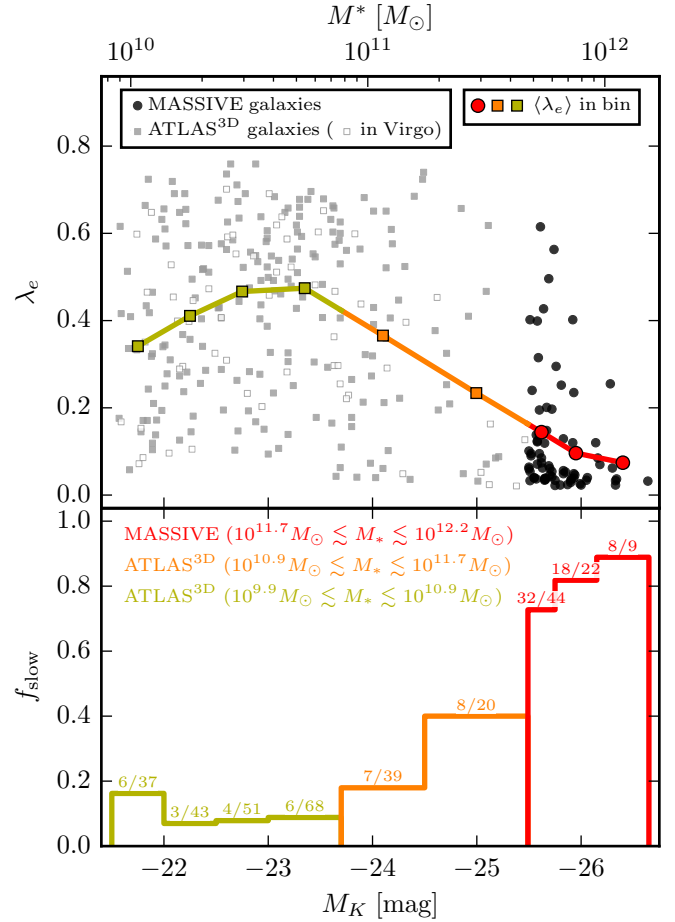


Figure 7. Spin parameter λ_e (top) and slow rotator fraction f_{slow} (bottom) versus M_* (and M_K) for MASSIVE (black circles) and ATLAS^{3D} galaxies (grey squares). The top panel shows that the MASSIVE and ATLAS^{3D} galaxies span a similar wide range of λ_e at $M_* \lesssim 10^{12} M_\odot$, but the mean λ_e (colour symbols) decreases sharply at high M_* . Open symbols indicate Virgo galaxies. We divide galaxies from the two surveys into three broad stellar mass bins indicated by red, orange and olive for analysis in Section 5.

used by ATLAS^{3D}) and Gauss-Hermite fits including higher moments (as we use) (van der Marel & Franx 1993).

4.2 λ_e versus M_*

We find a strong anti-correlation between λ_e and M_* , similar to our earlier finding from the smaller sample of 41 MASSIVE galaxies in (Veale et al. 2017). The top panel of Figure 7 shows λ_e versus M_* (and M_K) for each galaxy in MASSIVE and ATLAS^{3D}. Even though the range of λ_e at a given M_* is similar for almost the entire range of M_* , the average λ_e over 9 M_* bins (colour symbols) drops from ~ 0.4 for galaxies below $M_* \sim 10^{10.5} M_\odot$, to below 0.1 for galaxies above $M_* \sim 10^{12} M_\odot$. The bottom panel of Figure 7 plots the corresponding step rise in the fraction of slow rotators f_{slow} , from $\sim 10\%$ to $\sim 90\%$ with increasing M_* . The average behaviour of λ_e versus M_* in the top panel does not substantially change if we normalize λ_e by the slow/fast cutoff ($0.31\sqrt{\varepsilon}$). Some individual round galaxies have very high

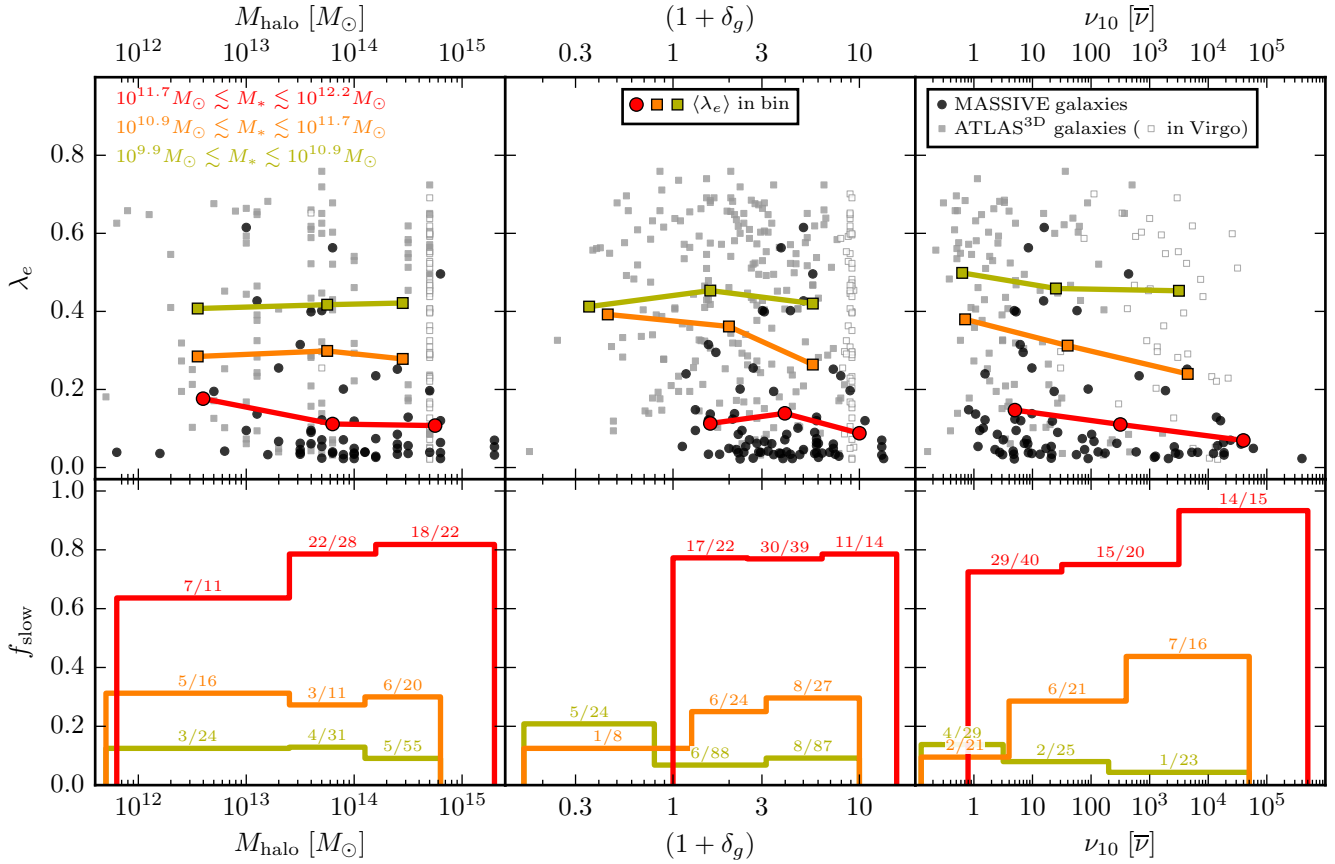


Figure 8. Spin parameter λ_e (top) and slow rotator fraction f_{slow} (bottom) as a function of M_{halo} (left), $1 + \delta_g$ (middle), and ν_{10} (right) for MASSIVE (black circles) and ATLAS^{3D} (grey squares) galaxies. Colour symbols and lines show the average λ_e (top) and f_{slow} (bottom) for three M_* bins. Overall, the average λ_e and f_{slow} both depend strongly on M_* , as shown in Figure 7. Within each M_* bin, however, both quantities vary little with M_{halo} , δ_g or ν_{10} . The most noticeable trend with environment is a decrease in the average λ_e (and an increase in f_{slow}) with increasing ν_{10} for the middle (orange) mass bin in the right panel.

normalized λ_e , but the average behaviour is qualitatively very similar.

There is a slight decrease in average λ_e and slight increase in f_{slow} at the low mass end of the ATLAS^{3D} sample. This is not due to any incompleteness of the sample (Capellari et al. 2011a), and also occurs if we use a flat cutoff to define the slow rotators, so it is not due to changes in ϵ influencing the classification. Perhaps coincidentally, the peak in the ETG mass function at $M_K \sim -22.5$ mag is near the peak of $\langle \lambda_e \rangle$ and the minimum of f_{slow} . It is also near the inferred peak in star formation efficiency at approximately $10^{10.5} M_\odot$ (e.g. Behroozi et al. 2013). Since we are focusing on the highest mass galaxies, we will not discuss these trends further.

5 GALAXY SPIN VERSUS ENVIRONMENT

In this section we examine the relation between galaxy spin and the various galaxy environmental measures defined in Section 3 for the combined MASSIVE and ATLAS^{3D} sample. Section 5.1 and Section 5.2 present simple tests of the correlation between slow rotator fraction f_{slow} and M_{halo} , δ_g , and ν_{10} , and Section 5.3 presents a more detailed test of how

the joint correlation of M_* vs. λ_e , and M_* vs. environment, impacts our results.

5.1 λ_e versus halo mass and density

Figure 8 shows the distribution of λ_e (upper panels) and f_{slow} (lower panels) versus halo mass M_{halo} (left), large-scale density contrast δ_g (middle), and local density ν_{10} (right). Measurements of λ_e for individual MASSIVE (black circles) and ATLAS^{3D} (grey squares) galaxies are shown in the upper panels. The colored lines show the average λ_e and f_{slow} for three M_* bins: $M_* > 10^{11.7} M_\odot$ (red) contains all MASSIVE galaxies in this study; and the other two bins contain ATLAS^{3D} galaxies with $10^{10.9} M_\odot < M_* < 10^{11.7} M_\odot$ (orange) and $10^{9.9} M_\odot < M_* < 10^{10.9} M_\odot$ (olive), respectively.

The average λ_e in Figure 8 is seen to decrease with increasing M_* bin, and f_{slow} is seen to increase correspondingly, as discussed in the previous section. Within each M_* bin, however, there is at most a weak correlation with environment. The lack of correlation applies regardless of the exact quantity we used to measure spin (i.e., individual λ_e , $\langle \lambda_e \rangle$, f_{slow}) or environment (i.e., M_{halo} , δ_g , ν_{10}). The MASSIVE galaxies occupy nearly the same range of λ_e , but have many more galaxies near $\lambda_e = 0$. Those slow and non-rotating

Table 2. p -values from KS test on slow and fast rotators. Small p -values indicate slow and fast rotators are likely drawn from different distributions in the given quantity. For the three environment measures we run the KS test separately on the two broad M_K bins of ATLAS^{3D}; M_K for each bin is given in magnitudes below.

	M_K	M_{halo}	δ_g	ν_{10}
MASSIVE (< -25.5)	0.314	0.305	0.710	0.414
ATLAS ^{3D} (-23.7 to -25.5)	0.007	0.835	0.156	0.112
ATLAS ^{3D} (> -23.7)		0.765	0.572	0.316
combined	10^{-8}	-	-	-

galaxies occupy the same range of environments as our overall sample, resulting in a low λ_e and high f_{slow} in all environments for our high-mass galaxies.

Some subtle trends with environment may be seen, although none are obviously significant given the number statistics of our samples, with one or two galaxies being the margin of difference in many cases. For MASSIVE galaxies, larger halo mass correlates with a slightly lower average λ_e and slightly higher f_{slow} (red lines in the left panels of Figure 8). Similar correlations also apply to ν_{10} for MASSIVE galaxies (red lines in the right panels of Figure 8), and to δ_g and ν_{10} for the more massive half of ATLAS^{3D} galaxies (orange lines in the middle and right panels of Figure 8).

To quantify the significance of these trends, we run two-sample Kolmogorov-Smirnov (KS) tests to compare the distribution of slow rotators to the distribution of fast rotators in M_{halo} , δ_g , and ν_{10} .² The resulting p -values for MASSIVE and ATLAS^{3D} are listed in Table 2. Many values are greater than 0.5, indicating that it is more likely than not that the slow and fast rotators are drawn from identical distributions in environment. The smallest p -values for environment are ~ 0.1 for the distributions in δ_g and ν_{10} of the more massive half of the ATLAS^{3D} galaxies. These align with the qualitative trends we noted above, but are still not considered significant. In comparison, a KS-test for the distribution of slow and fast rotators with M_K gives $p = 0.007$ for the ATLAS^{3D} sample, $p = 0.31$ for the MASSIVE sample, and approximately $p \sim 10^{-8}$ for a combined sample.³

² Because the KS test is not suitable for discrete parameters, the large number of ATLAS^{3D} galaxies at the same M_{halo} in Virgo (and to a lesser degree the duplicated M_{halo} values of other haloes for both surveys) causes a problem. To solve this, we add a small random variable between ± 0.1 to $\log_{10} M_{\text{halo}}$ before computing the KS test, and run 1000 trials of this procedure to find the average p -value.

³ For the combined sample, we copy each ATLAS^{3D} galaxy 10 times before finding the KS statistic to account for the fact that the MASSIVE volume is approximately 10 times larger. This gives a reasonable overall distribution in M_K , with no kink in the cumulative distribution function to inflate differences between the slow and fast rotators. To convert the KS statistic into a p -value, we use the original sample sizes, so the p -value is not artificially small due to artificially large N .

5.2 λ_e versus M_* , for two environmental bins

In the previous subsection we examined λ_e as a function of environment for three M_* bins. Here we investigate λ_e as a function of M_* for a low-density versus a high-density environmental bin.

Figure 9 shows the average λ_e versus M_* , split into two samples (orange versus blue) by each of our three environment measures: M_{halo} (left), δ_g (middle), and ν_{10} (right). The trend of λ_e with M_* for each environmental group in Figure 9 follows closely the trend of the whole sample in Figure 7. Within a M_* bin, however, there is again no statistically significant difference in the average λ_e for the higher versus lower density sample for any of the three environmental variables. In the central M_* bin, which spans a factor of ~ 5 in M_* ($10^{11} M_{\odot} < M_* < 10^{11.7} M_{\odot}$), the galaxies in the higher-density sample (orange) have a slightly higher average M_* and a lower average λ_e than the lower-density sample (blue). These points continue smoothly into the highest mass bins populated by the MASSIVE galaxies.

Like Figure 8, Figure 9 again illustrates that for local ETGs of similar M_* , the galaxy spin does not correlate noticeably with galaxy environment.

5.3 λ_e , M_* , and environment

We perform an additional test to gain further insight into the lack of correlation between galaxy spin and environment at fixed stellar mass. We create a randomized sample in which the galaxies' M_* and environment are preserved but the spins are shuffled. Specifically, we randomly assign each galaxy to be a fast or slow rotator, using the probability for being a slow rotator determined by the galaxy's M_* shown in Figure 7 (bottom panel). For example, a galaxy with $M_* = 10^{10.6} M_{\odot}$ has a $6/68 = 8.8\%$ chance of being a slow rotator, and a galaxy with $M_* = 10^{12.1} M_{\odot}$ has a $8/9 = 89\%$ chance of being a slow rotator, independent of their environment. We then count the fraction of slow rotators in each environment for each survey, and repeat the procedure 1000 times to obtain an estimate of the fraction and error bar⁴ that reflects expected errors due to small sample sizes. We estimate error bars on the observed f_{slow} with a Bayesian method described in Appendix B.

Figure 10 shows f_{slow} for this test sample (symbols with black error bars) for three M_* bins for the three types of group memberships (isolated, satellite and BGG). The fact that the randomized test sample reproduces the observed f_{slow} supports our finding of the lack of an independent correlation between galaxy spin and environment as quantified by group membership. The much higher fraction of slow rotators in MASSIVE (red) than ATLAS^{3D} galaxies (orange and olive) seen in Figure 10 arises from their higher M_* and not galaxy environment. Likewise, the increasing fraction of slow rotators with group membership category for ATLAS^{3D} galaxies can be accounted for entirely (within errors) by the joint correlations between M_* and spin, and between M_* and environment.

Figure 11 shows the same comparison as Figure 10 but

⁴ The 68% confidence interval based on the cumulative distribution function of trials.

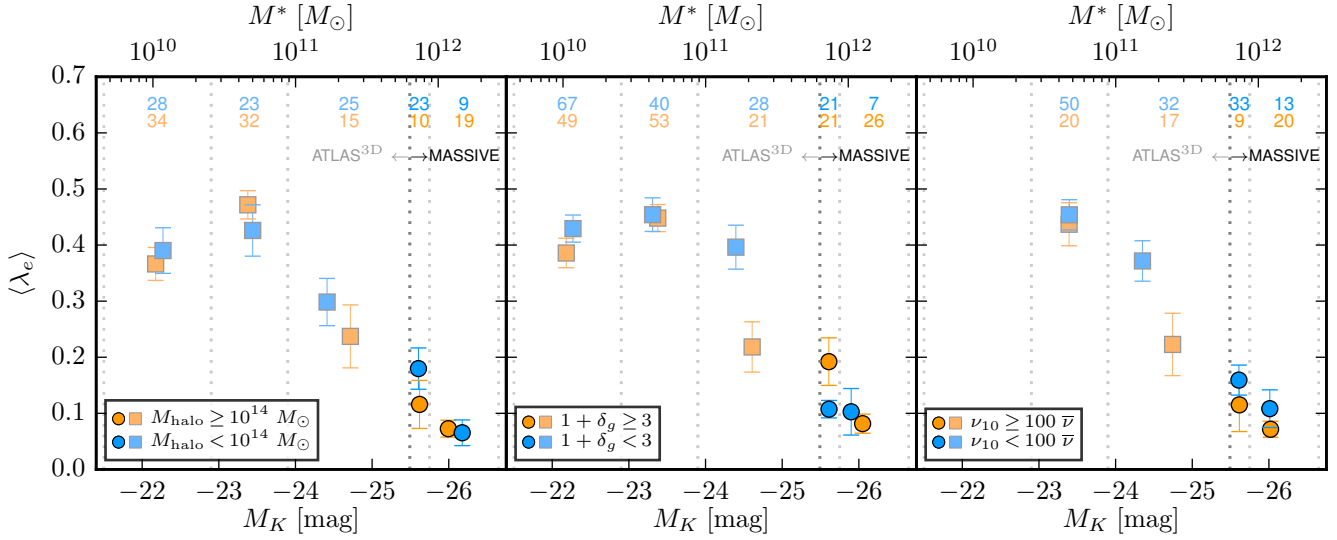


Figure 9. Average λ_e in bins of M_* (demarcated by dotted lines) for MASSIVE (circles) and ATLAS^{3D} (squares) galaxies. Within each M_* bin, the average of λ_e is taken over two subsamples, one for galaxies in denser environments (orange) and one for less dense environments (blue); the corresponding number of galaxies is listed at the top of each bin. From left to right, the panels show splits by M_{halo} , δ_g , and ν_{10} . (We do not calculate ν_{10} for galaxies with $M_K > -23.0$ mag; see Appendix A for details.) Each $\langle \lambda_e \rangle$ point is placed at the average M_* for the galaxies in that environmental bin. While the orange point is significantly lower than the blue point in the highest mass ATLAS^{3D} bin ($10^{11} M_\odot \lesssim M_* \lesssim 10^{11.7} M_\odot$), it is also at a higher average M_* than the blue point. Altogether, the decrease in the average λ_e with M_* continues smoothly from the ATLAS^{3D} sample to the MASSIVE sample. There is no evidence that galaxies at the same M_* but with different environments have different rotation properties.

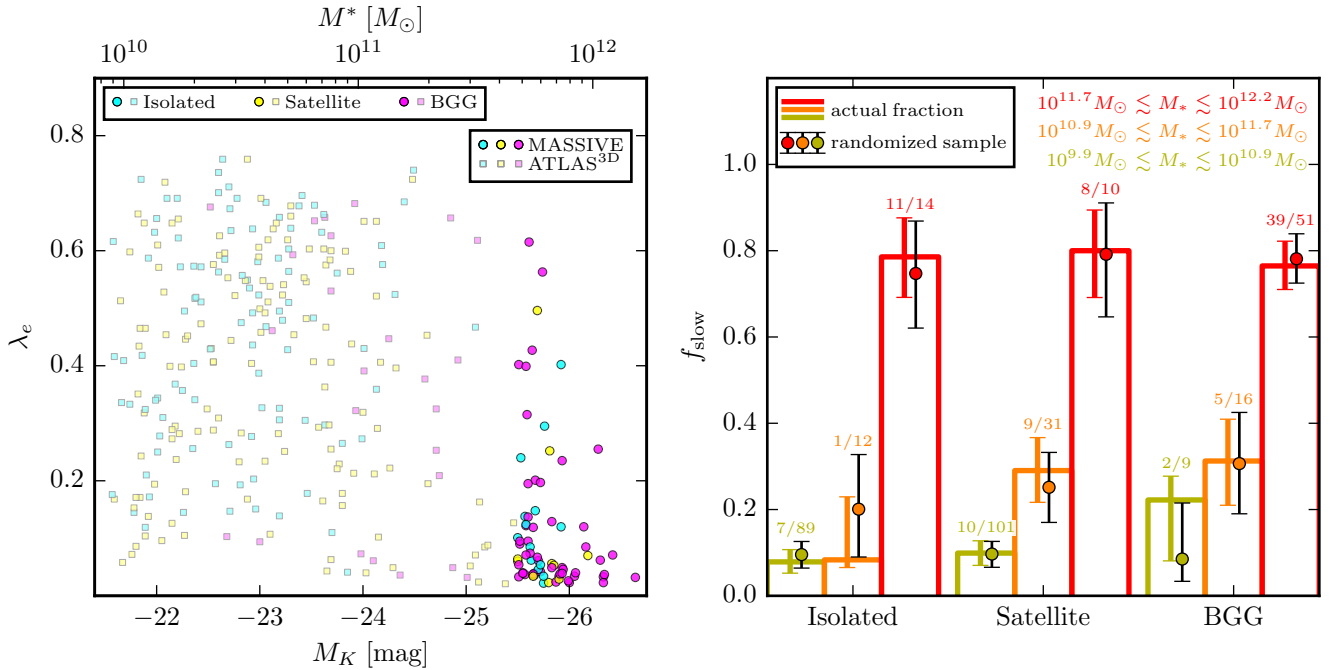


Figure 10. λ_e versus M_* (left) and f_{slow} (right) divided by group membership status for MASSIVE and ATLAS^{3D} galaxies. BGG galaxies (magenta) tend to have higher M_* than isolated (cyan) and satellite (yellow) galaxies. Combined with the increasing f_{slow} at higher mass, this results in a higher f_{slow} (right panel) among BGG galaxies in the more massive ATLAS^{3D} mass bin (orange). The trend holds, within errors, even when the slow/fast classification of each galaxy is randomized within each M_* bin (symbols with black error bars; see text for details).

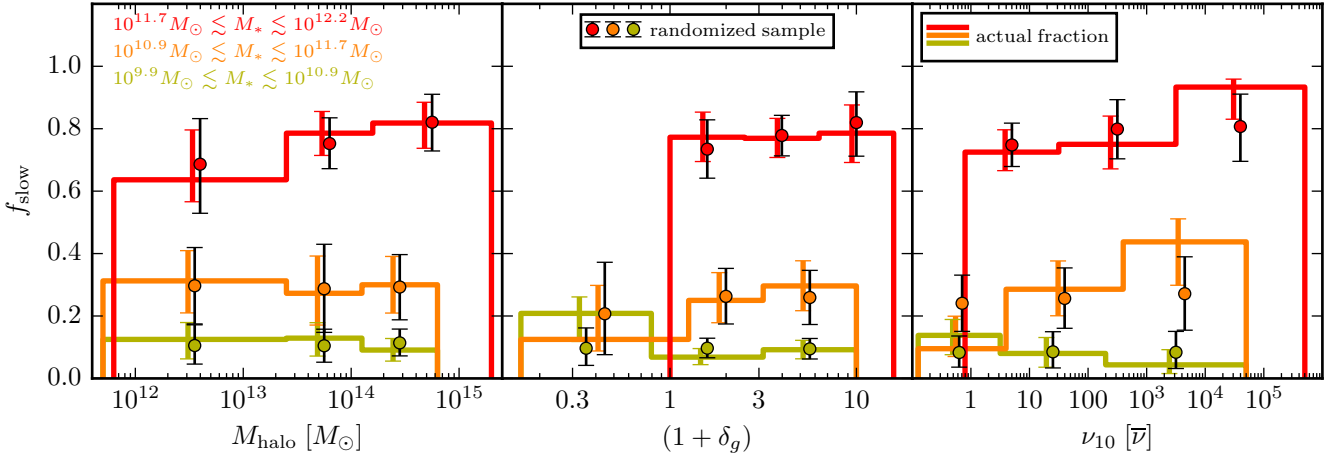


Figure 11. Same as the bottom panels of Figure 8 for f_{slow} versus M_{halo} (left), δ_g (middle), and ν_{10} (right). In each panel, the randomized test sample (symbols with black error bars) matches very well the observed f_{slow} (histograms with colour error bars). A possible exception is that the observed f_{slow} may have a steeper correlation with ν_{10} than the randomized sample, for the MASSIVE galaxies (red) and the more massive half of the ATLAS^{3D} galaxies (orange).

for the other environmental measures. The observed trends of f_{slow} with environment for the three M_* bins is again reproduced in the test sample despite the randomization of galaxy spin. One possible exception is the highest ν_{10} bin for the middle and high mass bins (orange and red in the right panel of Figure 11), where the test sample underpredicts the observed f_{slow} slightly. For completeness, we also apply this procedure to the local densities ν_{10} and Σ_3 originally tabulated in Cappellari et al. (2011b) (see Appendix C) and obtain similar results.

Figure 10 and Figure 11 show that the observed f_{slow} match closely the test samples in which galaxy spin and environment are randomized. We therefore conclude that there is likely little or no correlation between spin and environment for galaxies of the same mass, and the apparent kinematic morphology-density is largely driven by stellar mass.

6 CONCLUSIONS

In this paper we have analysed the detailed environmental properties of the 116 galaxies in the MASSIVE survey and the 260 galaxies in the ATLAS^{3D} survey. The MASSIVE survey is designed to sample a much larger volume than ATLAS^{3D} and to target exclusively galaxies above $M_* = 10^{11.5} M_\odot$; only 6 ATLAS^{3D} galaxies are above this mass limit (Section 2). These two complementary IFS surveys together span $-21.5 \gtrsim M_K \gtrsim -26.6$ mag, or $8 \times 10^9 \lesssim M_* \lesssim 2 \times 10^{12} M_\odot$, and provide the most comprehensive study to date of individual early-type galaxies in the local universe.

We examined different ways to quantify galaxy environment and presented results for group membership (BGG, satellite or isolated), halo mass, large-scale density δ_g measured over a few Mpc, and local density ν_{10} measured within the 10th nearest neighbour of each galaxy (Section 3). Despite their high stellar masses, MASSIVE galaxies reside in a diverse range of environments, and not all of them are the brightest galaxies in massive haloes at high densities, as is

commonly assumed for massive ETGs. This key feature of massive galaxies was highlighted in Ma et al. (2014); here we have added environmental measures δ_g and ν_{10} to the analysis. About 20% of MASSIVE galaxies are “isolated”, having fewer than three group members in the 2MASS HDC catalogue (Figure 2); about 30% of MASSIVE galaxies are in regions of modest densities $\nu_{10} \lesssim 10\bar{\nu}$, or $\delta_g \lesssim 2$ (Figure 3). Compared to ATLAS^{3D} galaxies, we found a higher fraction of MASSIVE galaxies to be BGGs ($\sim 60\%$ versus 10%) and to be located in more massive haloes and higher density regions (Figure 2 and Figure 3).

We then presented measurements of galaxy spin λ_e for the 75 galaxies of the MASSIVE “priority sample” with IFS data (Section 4). We confirm the strong anti-correlation between spin and stellar mass that we reported earlier for a smaller sample of MASSIVE galaxies (Veale et al. 2017): the average λ_e decreases from ~ 0.4 at $M_* \sim 10^{10} M_\odot$ to below 0.1 at $M_* \gtrsim 10^{12} M_\odot$, and the fraction of slow rotators increases from $\sim 10\%$ to 90% (Figure 7).

The combined MASSIVE and ATLAS^{3D} sample is sufficiently large for us to analyze for the first time the correlation between galaxy spin and environment – the so-called kinematic morphology-density relation – at fixed M_* . After controlling for M_* , we found almost no remaining correlations between galaxy environment and spin (Figure 8–Figure 11).

In particular, we find a high fraction of slow rotators ($\sim 80\%$) in the MASSIVE sample in every environment, regardless of group membership, halo mass, or densities δ_g or ν_{10} (Figure 8, Figure 10 and Figure 11). Previous studies did not include high-mass galaxies at low environmental densities since they either sampled smaller volumes (Cappellari et al. 2011b) or investigated only individual clusters (D’Eugenio et al. 2013; Houghton et al. 2013; Fogarty et al. 2014). Strong correlations between slow rotator fraction and local density have been reported for these samples, with possible implications for slow rotator formation pathways (see, e.g. Cappellari 2016 for a review). However, without the high-mass low-density galaxies like those in the

MASSIVE survey, it was difficult to assess whether the kinematic morphology-density relation applies at fixed mass, i.e., whether environmental overdensities play a role in the formation of slow rotators that is distinct from their role as a natural environment for massive ETGs in general. The results presented in this paper show that a dense environment is not required to create massive slow rotators.

Our tests show that most observed correlations between galaxy environment and spin can be explained by the joint connections between M_* and spin, and between M_* and environment (Figure 9, Figure 11). This is consistent with a scenario in which mergers generally are responsible for both increasing the mass of a galaxy and decreasing the spin. A possible exception is the local density ν_{10} , which shows evidence that the highest densities host a slightly larger fraction of slow rotators, even after controlling for M_* (Figure 11). This residual dependence may indicate that certain types of assembly history – perhaps those including more minor mergers and non-merger interactions as suggested by simulations (e.g., Moody et al. 2014; Choi & Yi 2017) – are more likely to create slow rotators, even when controlling for the final mass of the galaxy, and that local density is a reasonable proxy for the type of assembly history.

The fast-slow kinematic transformation (e.g. this work, Cappellari 2013) can be compared to the spiral-elliptical morphological transformation (e.g. Dressler 1980). Galaxy kinematics and morphologies both transform with galaxy mass, so it is important to examine whether the transformation with environment applies at fixed mass. The morphology-density relation nearly disappears for galaxy samples at fixed stellar mass (e.g., Bamford et al. 2009; Tasca et al. 2009; Blanton & Moustakas 2009; Grützbauch et al. 2011; Muzzin et al. 2012; Alpaslan et al. 2015; Saracco et al. 2017). We have found the same to be true for the kinematic morphology-density relation, which, at fixed stellar mass, disappears completely for every environmental measure studied in this paper except perhaps ν_{10} . A recent preprint finds similar results for galaxies in eight clusters with halo mass above $10^{14.2} M_\odot$ from the SAMI survey, with no significant remaining relationship between the slow rotator fraction and local overdensity after controlling for the strong correlation with mass (Brough et al. 2017).

Increased statistics from ongoing and future surveys using IFS such as SAMI (Croom et al. 2012), CALIFA (Sánchez et al. 2012), MaNGA (Bundy et al. 2015), and HECTOR (Bryant et al. 2016) could provide more sensitive probes of the transition regime between fast and slow rotating ETGs. The MASSIVE survey is designed to explore new parameter space unprobed by ATLAS^{3D}; the two samples therefore have little overlap. It is somewhat a coincidence that ETGs transition from being dominated by fast rotators to being dominated by slow rotators at $M_K \sim -25$ mag, the interface between the two surveys (Figure 7). A volume-limited survey targeting more galaxies brighter than $M_K \sim -24$ mag would be useful for gaining further insight into the kinematic transformation along the mass sequence of present-day ETGs.

ACKNOWLEDGEMENTS

We thank Mike Hudson for his assistance with the 2M++ catalogue. The MASSIVE survey is supported in part by NSF AST-1411945, NSF AST-1411642, HST-GO-14210, and HST-AR-1457.

REFERENCES

- Abazajian K. N., et al., 2009, *ApJS*, **182**, 543
 Aihara H., et al., 2011, *ApJS*, **193**, 29
 Alpaslan M., et al., 2015, *MNRAS*, **451**, 3249
 Bahcall J. N., Tremaine S., 1981, *ApJ*, **244**, 805
 Baldry I. K., Glazebrook K., Brinkmann J., Ivezić Ž., Lupton R. H., Nichol R. C., Szalay A. S., 2004, *ApJ*, **600**, 681
 Bamford S. P., et al., 2009, *MNRAS*, **393**, 1324
 Behroozi P. S., Wechsler R. H., Conroy C., 2013, *ApJ*, **770**, 57
 Bender R., Surma P., Doebereiner S., Moellenhoff C., Madejsky R., 1989, *A&A*, **217**, 35
 Blakeslee J. P., 2013, in de Grijs R., ed., *IAU Symposium Vol. 289*, IAU Symposium. pp 304–311, doi:10.1017/S174392131202159X
 Blakeslee J. P., et al., 2009, *ApJ*, **694**, 556
 Blakeslee J. P., et al., 2010, *ApJ*, **724**, 657
 Blanton M. R., Moustakas J., 2009, *ARA&A*, **47**, 159
 Blanton M. R., Roweis S., 2007, *AJ*, **133**, 734
 Bois M., et al., 2011, *MNRAS*, **416**, 1654
 Brough S., et al., 2017, preprint, (arXiv:1704.01169)
 Bryant J. J., et al., 2016, preprint, (arXiv:1608.03921)
 Bundy K., et al., 2015, *ApJ*, **798**, 7
 Cappellari M., 2013, *ApJ*, **778**, L2
 Cappellari M., 2016, *ARA&A*, **54**, 597
 Cappellari M., Emsellem E., 2004, *PASP*, **116**, 138
 Cappellari M., et al., 2011a, *MNRAS*, **413**, 813
 Cappellari M., et al., 2011b, *MNRAS*, **416**, 1680
 Carollo C. M., et al., 2013, *ApJ*, **776**, 71
 Carrick J., Turnbul S. J., Lavaux G., Hudson M. J., 2015, *MNRAS*, **450**, 317
 Choi H., Yi S., 2017, preprint, (arXiv:1702.00517)
 Crook A. C., Huchra J. P., Martimbeau N., Masters K. L., Jarrett T., Macri L. M., 2007, *ApJ*, **655**, 790
 Crook A. C., Huchra J. P., Martimbeau N., Masters K. L., Jarrett T., Macri L. M., 2008, *ApJ*, **685**, 1320
 Croom S. M., et al., 2012, *MNRAS*, **421**, 872
 D’Eugenio F., Houghton R. C. W., Davies R. L., Dalla Bontà E., 2013, *MNRAS*, **429**, 1258
 Davies R. L., Burstein D., Dressler A., Faber S. M., Lynden-Bell D., Terlevich R. J., Wegner G., 1987, *ApJS*, **64**, 581
 Djorgovski S., Davis M., 1987, *ApJ*, **313**, 59
 Dressler A., 1980, *ApJ*, **236**, 351
 Dressler A., Lynden-Bell D., Burstein D., Davies R. L., Faber S. M., Terlevich R., Wegner G., 1987, *ApJ*, **313**, 42
 Durrell P. R., et al., 2014, *ApJ*, **794**, 103
 Emsellem E., et al., 2007, *MNRAS*, **379**, 401
 Emsellem E., et al., 2011, *MNRAS*, **414**, 888
 Falco M., Hansen S. H., Wojtak R., Brinckmann T., Lindholmer M., Pandolfi S., 2014, *MNRAS*, **442**, 1887
 Ferrarese L., et al., 2012, *ApJS*, **200**, 4
 Fogarty L. M. R., et al., 2014, *MNRAS*, **443**, 485
 Grützbauch R., Conselice C. J., Varela J., Bundy K., Cooper M. C., Skibba R., Willmer C. N. A., 2011, *MNRAS*, **411**, 929
 Heisler J., Tremaine S., Bahcall J. N., 1985, *ApJ*, **298**, 8
 Hill G. J., et al., 2008, in *Society of Photo-Optical Instrumentation Engineers (SPIE) Conference Series.*, doi:10.1117/12.790235
 Hoffman L., Cox T. J., Dutta S., Hernquist L., 2010, *ApJ*, **723**, 818

Houghton R. C. W., et al., 2013, *MNRAS*, **436**, 19

Huchra J., et al., 2005a, in Colless M., Staveley-Smith L., Stathakis R. A., eds, IAU Symposium Vol. 216, Maps of the Cosmos. p. 170

Huchra J., et al., 2005b, in Fairall A. P., Woudt P. A., eds, Astronomical Society of the Pacific Conference Series Vol. 329, Nearby Large-Scale Structures and the Zone of Avoidance. p. Fairall

Huchra J. P., et al., 2012, *ApJS*, **199**, 26

Illingworth G., 1977, *ApJ*, **218**, L43

Jarrett T. H., Chester T., Cutri R., Schneider S., Skrutskie M., Huchra J. P., 2000, *AJ*, **119**, 2498

Jimmy Tran K.-V., Brough S., Gebhardt K., von der Linden A., Couch W. J., Sharp R., 2013, *ApJ*, **778**, 171

Jones D. H., et al., 2009, *MNRAS*, **399**, 683

Khochfar S., et al., 2011, *MNRAS*, **417**, 845

Kormendy J., Bender R., 1996, *ApJ*, **464**, L119

Kormendy J., Fisher D. B., Cornell M. E., Bender R., 2009, *ApJS*, **182**, 216

Kubo J. M., Stebbins A., Annis J., Dell'Antonio I. P., Lin H., Khiabani H., Frieman J. A., 2007, *ApJ*, **671**, 1466

Lauer T. R., 2012, *ApJ*, **759**, 64

Lauer T. R., et al., 2007, *ApJ*, **662**, 808

Lavaux G., Hudson M. J., 2011, *MNRAS*, **416**, 2840

Ma C.-P., Greene J. E., McConnell N., Janish R., Blakeslee J. P., Thomas J., Murphy J. D., 2014, *ApJ*, **795**, 158

Martizzi D., Jimmy Teyssier R., Moore B., 2014, *MNRAS*, **443**, 1500

Moody C. E., Romanowsky A. J., Cox T. J., Novak G. S., Primack J. R., 2014, *MNRAS*, **444**, 1475

Mould J. R., et al., 2000, *ApJ*, **529**, 786

Muldrew S. I., et al., 2012, *MNRAS*, **419**, 2670

Muzzin A., et al., 2012, *ApJ*, **746**, 188

Naab T., et al., 2014, *MNRAS*, **444**, 3357

Oliva-Altamirano P., et al., 2017, *AJ*, **153**, 89

Penoyre Z., Moster B. P., Sijacki D., Genel S., 2017, preprint, ([arXiv:1703.00545](https://arxiv.org/abs/1703.00545))

Rines K., Geller M. J., Kurtz M. J., Diaferio A., 2003, *AJ*, **126**, 2152

Sánchez S. F., et al., 2012, *A&A*, **538**, A8

Saracco P., Gargiulo A., Ciocca F., Marchesini D., 2017, *A&A*, **597**, A122

Schindler S., Binggeli B., Böhringer H., 1999, *A&A*, **343**, 420

Schombert J., Smith A. K., 2012, *Publ. Astron. Soc. Australia*, **29**, 174

Scott N., Davies R. L., Houghton R. C. W., Cappellari M., Graham A. W., Pimblet K. A., 2014, *MNRAS*, **441**, 274

Simionescu A., et al., 2011, *Science*, **331**, 1576

Skibba R. A., van den Bosch F. C., Yang X., More S., Mo H., Fontanot F., 2011, *MNRAS*, **410**, 417

Skrutskie M. F., et al., 2006, *AJ*, **131**, 1163

Tasca L. A. M., et al., 2009, *A&A*, **503**, 379

Thomas D., Maraston C., Bender R., Mendes de Oliveira C., 2005, *ApJ*, **621**, 673

Veale M., et al., 2017, *MNRAS*, **464**, 356

Vulcani B., et al., 2016, *ApJ*, **816**, 86

York D. G., Adelman J., Anderson Jr. J. E., Anderson S. F., Annis J., Bahcall N. A., et al., 2000, *AJ*, **120**, 1579

van der Marel R. P., Franx M., 1993, *ApJ*, **407**, 525

APPENDIX A: CALCULATION OF ν_{10}

The local luminosity density ν_{10} was described briefly in Section 3.4. Here we discuss some of the technical details of

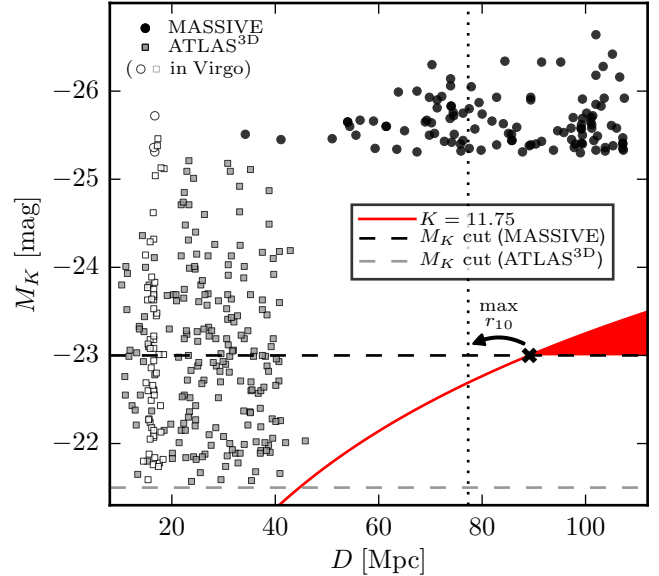


Figure A1. Schematic of the magnitude limits of 2MRS (red line), the ATLAS^{3D} sample (grey squares) and its parent sample (dashed grey line), and the MASSIVE sample (black circles) and its parent sample (dashed black line) defined for the purposes of calculating ν_{10} . Galaxies in the MASSIVE volume that should be in the parent sample but are fainter than the 2MRS survey limit (red shaded region) may cause ν_{10} to be under-estimated. Because r_{10} , the distance to the 10th neighbour, can be as large as ~ 10 Mpc, this extends the potential impact of the incomplete region significantly beyond the intersection of the M_K cut and $K = 11.75$ mag to all galaxies to the right of the dotted line. Moving the cut for the MASSIVE parent sample up moves the dotted line to the right, meaning fewer galaxies impacted by incompleteness; however, it also causes more ATLAS^{3D} galaxies to fall outside the cut. Our choice of $M_K < -23.0$ mag is a compromise between those competing effects.

calculating ν_{10} , which is defined as follows:

$$\nu_{10} = \frac{\sum_{i=0}^{10} 10^{-0.4(M_{i,K} - M_{\odot,K})}}{\frac{4}{3}\pi r_{10}^3} \quad (\text{A1})$$

where the solar K -band luminosity is $M_{\odot,K} = 3.29$ mag (Blanton & Roweis 2007). Index $i = 0$ to 10 refers to the galaxy itself ($i = 0$) and its ten nearest neighbours, so r_{10} is the distance to the 10th neighbour and defines a sphere containing the 10 neighbours.

In Cappellari et al. (2011b), the ten nearest neighbours were chosen from the ATLAS^{3D} parent sample, containing all galaxies (not just ETGs) in the ATLAS^{3D} volume with $M_K < -21.5$ mag. This cut reflects the 2MRS survey limit of $K = 11.75$, which is illustrated in Figure A1. Using the same M_K cut to define a parent sample for MASSIVE would result in substantial incompleteness; all galaxies between the red line and dashed grey line in Figure A1 would be missing. On the other hand, to guarantee zero impact from incompleteness to our ν_{10} calculation (moving the vertical dotted line all the way to the right of the figure) would require a cut of $M_K < -24.0$, which would cause most ATLAS^{3D} galaxies to fall outside the cut entirely. We want to make a fair comparison to ATLAS^{3D} galaxies, so we recompute

ν_{10} instead of using the values in Cappellari et al. (2011b), and thus want to keep more than a few galaxies inside our cut. We choose to define the MASSIVE parent sample with $M_K < -23.0$ as a compromise between those two considerations. This cut allows us to keep about half of the ATLAS^{3D} galaxies for comparison, while about half of the MASSIVE galaxies have ν_{10} possibly impacted by incompleteness of the parent sample.

To estimate the impact of incompleteness on ν_{10} , we repeated our calculation for a parent sample cut at $M_K < -24.0$. Using only galaxies not impacted by incompleteness (i.e. those to the left of the dotted line in Figure A1), we found that expanding the parent sample from $M_K < -24.0$ to $M_K < -23.0$ results in a characteristic increase of $\Delta \log_{10} \nu_{10} \sim 0.6$. This represents a worst case scenario for the bias in ν_{10} of galaxies to the right of the dotted line, since only those at the very edge of the volume experience the maximum effect of incompleteness. Since ν_{10} covers six orders of magnitude, we judge this to be a minor impact.

Another difference between the MASSIVE and ATLAS^{3D} surveys is the availability of accurate distance estimates (discussed in detail in Ma et al. 2014 and Cappellari et al. 2011a respectively). For most of the MASSIVE galaxies, we use group distances from the catalogues of Crook et al. (2007). This effectively flattens the galaxies in each group to the same distance, and would generally result in a higher ν_{10} . Although more accurate distances would result in more accurate values of ν_{10} , we wish to make a fair comparison to ATLAS^{3D} galaxies, so we do not use the accurate distances tabulated by the survey papers even when they are available. Instead, we assign distances from the HDC catalogue first (if available), then from the LDC catalogue, and as a last resort use the raw 2MRS redshift distance.

Figure A2 compares our recalculated ν_{10} to the values from Cappellari et al. (2011b). Overall the agreement is reasonable, considering the two competing influences of our changes to the calculation. First, we have a more strict M_K cut on the parent sample, which will reduce ν_{10} . We see this at low densities, with reductions in ν_{10} up to an order of magnitude. This is roughly in line with our comparison between the $M_K < -24.0$ and $M_K < -23.0$ cuts discussed above. Second, we have ignored accurate distance estimates for nearby galaxies in favor of a more uniform assignment of group distances. Flattening the groups to a single distance reshuffles the order of which neighbouring galaxies are closest, which may have a small impact on the total luminosity, but the major impact on ν_{10} comes from reduced r_{10} . Even if the 10 neighbours are the same galaxies, r_{10} is reduced to a 2-dimensional R_{10} if all neighbours are in the same group. It can be reduced further if galaxies that are nearly coincident on-sky, but are at opposite sides of the group along the line of sight, are counted as neighbours when they would not be otherwise. A moderate change in r_{10} has an impact of r^3 on the volume used to calculate ν_{10} , and in a very few cases ν_{10} increases by up to 2 orders of magnitude.

The agreement between our new ν_{10} and the original values is good, considering the effects described above. We also stress that enabling a fair comparison between MASSIVE and ATLAS^{3D} galaxies is more important than increased accuracy of ν_{10} for individual galaxies.

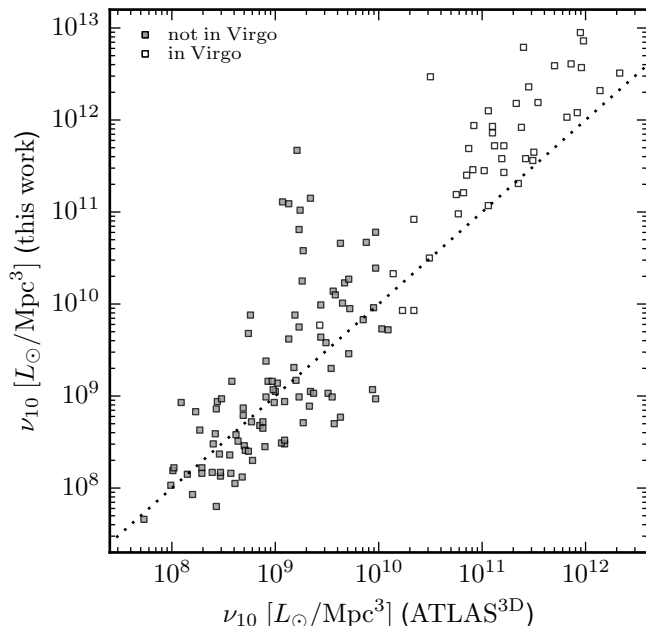


Figure A2. Our recalculated ν_{10} versus the ν_{10} from Cappellari et al. (2011b) for ATLAS^{3D} galaxies. At low density, we see the effect of our more strict M_K cut, resulting in a lower ν_{10} for most galaxies. Within groups and clusters, flattening each group to a single distance can result in somewhat reduced r_{10} , which results in significantly increased ν_{10} for a few galaxies.

APPENDIX B: BAYESIAN ERROR ESTIMATES FOR FRACTION OF SLOW ROTATORS

In Section 5.3 we compare the observed fraction of slow rotators f_{slow} as a function of environment to what we predict using M_K . There is limited statistical power in certain bins, where the number of MASSIVE and/or ATLAS^{3D} galaxies is small. Thus we require a reasonable estimate of the error on f_{slow} so that we can make the comparison fairly and not overstate any differences.

For simplicity, we will ignore error bars on λ_e and treat the classification of each individual galaxy as slow or fast as a 100% certain measurement with no errors. Although this is not true, the statistical errors due to sample size are our main concern. The fraction of slow rotators must be between 0 and 1, and many simple estimates of the error are unsatisfactory. (For example, a simple bootstrapping method would yield zero error for a subsample of 5 galaxies containing 0 slow rotators, even though there should be significant uncertainty due to the small sample size.) Fortunately, our problem is equivalent to a well known example in Bayesian statistics, the problem of flipping a biased coin N times and estimating the true probability of getting heads or tails.

For some fraction of coin flips (or slow rotators) x , the prior and posterior distributions can be conveniently defined by a Beta distribution:

$$P(x) \propto x^{\alpha-1}(1-x)^{\beta-1} \quad (\text{B1})$$

with a mean of $\mu = \alpha/(\alpha + \beta)$. The quantity $n = \alpha + \beta$ is often interpreted as the sample size, and the variance is $\mu(1-\mu)/(n+1)$. The parameters of the posterior distribution, given a prior distribution and the measured numbers of fast and

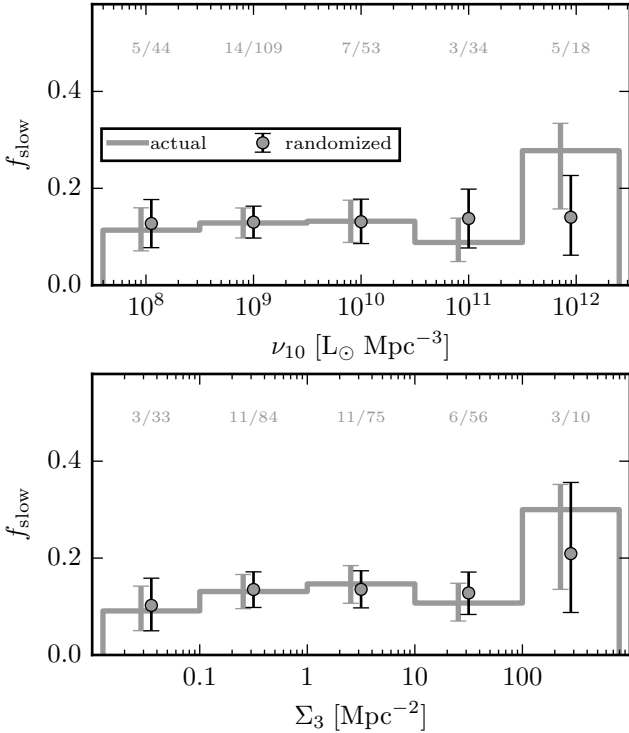


Figure C1. Slow rotator fraction f_{slow} versus ν_{10} and Σ_3 for ATLAS^{3D} galaxies, using densities originally tabulated in Cappellari et al. (2011b). While the observed f_{slow} appears similar in both cases, rising in the highest density bin, comparing to f_{slow} in the randomized sample (see Section 5.3) shows an important difference. The slow fraction as a function of Σ_3 is nearly identical when randomized within bins of M_K , but for ν_{10} the randomized sample underpredicts f_{slow} in the highest bin.

slow rotators, are $\alpha_{\text{post}} = \alpha_{\text{prior}} + N_{\text{slow}}$, $\beta_{\text{post}} = \beta_{\text{prior}} + N_{\text{total}} - N_{\text{slow}}$.

We choose a prior distribution based on f_{slow} for each survey: $\mu_{\text{prior}} = 0.78$ for MASSIVE and $\mu_{\text{prior}} = 0.13$ for ATLAS^{3D}, with $n_{\text{prior}} = 5$ for both. Then to obtain the error on f_{slow} in each specific bin of environment, we find the 68% confidence interval of the posterior distribution. These choices of prior are somewhat arbitrary (i.e. there is nothing special about $n_{\text{prior}} = 5$), but qualitatively give the behaviour we expect. We have a weak prior assumption that any subsample of galaxies will have the same f_{slow} as the overall sample, so the errors will be slightly asymmetric towards that overall fraction, and the size of the error depends properly on the size of the subsample. The slow fraction for ATLAS^{3D} BGG galaxies in the bottom panel of Figure 10 is a good illustration of these properties.

APPENDIX C: COMPARING TO ATLAS^{3D} DENSITIES

Figure C1 compares the observed slow rotator fraction f_{slow} to the test sample constructed by randomizing the slow/fast assignment of galaxies within bins of M_K . (See Section 5.3 for details.) This is similar to the results shown in Figure 11, but uses the local densities ν_{10} and Σ_3 tab-

ulated in Cappellari et al. (2011b) for the ATLAS^{3D} sample. The results in the top panel of Figure C1 for the entire ATLAS^{3D} sample, with ν_{10} calculated using the best available distance estimates, are slightly different from the results in the top right panel of Figure 11, calculated for galaxies with $M_K < -23.0$ using our simplified distances.

Both measures of local density find an increase in f_{slow} in the highest density bin, but the test samples (grey points in Figure C1) show an important difference. The slow rotator fraction as a function of Σ_3 is well matched using the randomized test sample, but in the case of ν_{10} the test sample underpredicts f_{slow} at the highest bin. This is very similar to the results for MASSIVE galaxies in the top right panel of Figure 11.

This paper has been typeset from a $\text{\TeX}/\text{\LaTeX}$ file prepared by the author.